Draft version November 4, 2010
Preprint typeset using LaTeX style emulateapj v. 11/10/09

SPIRALLING OUT OF CONTROL: 3D HYDRODYNAMICAL MODELLING OF THE COLLIDING WINDS IN η CARINAE

E. R. Parkin[1,2,6] J. M. Pittard[2], M. F. Corcoran[3,4], and K. Hamaguchi[3,5]

[1]Institut d'Astrophysique et de Géophysique, Université de Liège, 17, Allée du 6 Août, B5c, B-4000 Sart Tilman, Belgium
[2]School of Physics and Astronomy, The University of Leeds, Woodhouse Lane, Leeds LS2 9JT, UK
[3]CRESST and X-ray Astrophysics Laboratory, NASA/GSFC, Greenbelt, MD 20771, USA
[4]Universities Space Research Association, 10211 Wisconsin Circle, Suite 500 Columbia, MD 21044, USA
[5]Department of Physics, University of Maryland, Baltimore County, 1000 Hilltop Circle, Baltimore, MD 21250, USA and
[6]Current address: Research School of Astronomy and Astrophysics, Mount Stromlo Observatory, Australian National University, Cotter Road, Weston Creek, ACT 2611, Australia

Draft version November 4, 2010

ABSTRACT

Three dimensional (3D) adaptive-mesh refinement (AMR) hydrodynamical simulations of the wind-wind collision between the enigmatic super-massive star η Car and its mysterious companion star are presented which include radiative driving of the stellar winds, gravity, optically-thin radiative cooling, and orbital motion. Simulations with static stars with a periastron passage separation reveal that the preshock companion star's wind speed is sufficiently reduced that radiative cooling in the postshock gas becomes important, permitting the runaway growth of non-linear thin shell (NTSI) instabilities which massively distort the WCR. However, large-scale simulations which include the orbital motion of the stars, show that orbital motion reduces the impact of radiative inhibition, and thus increases the acquired preshock velocities. As such, the postshock gas temperature and cooling time see a commensurate increase, and sufficient gas pressure is preserved to stabilize the WCR against catastrophic instability growth. We then compute synthetic X-ray spectra and lightcurves and find that, compared to previous models, the X-ray spectra agree much better with *XMM-Newton* observations just prior to periastron. The narrow width of the 2009 X-ray minimum can also be reproduced. However, the models fail to reproduce the extended X-ray mimimum from previous cycles. We conclude that the key to explaining the extended X-ray minimum is the rate of cooling of the companion star's postshock wind. If cooling is rapid then powerful NTSIs will heavily disrupt the WCR. Radiative inhibition of the companion star's preshock wind, albeit with a stronger radiation-wind coupling than explored in this work, could be an effective trigger.

Subject headings: hydrodynamics - stars:early-type - X-rays:stars - stars:binaries - stars:winds, outflows - stars:individual(η Carinae)

1. INTRODUCTION

Of the known massive stars in our galaxy, η Car is possibly the largest and finest example of a pre-hypernova candidate, presenting a rare but exceptional opportunity to test our current understanding of stellar evolution in the upper Hertzsprung-Russell diagram. Yet, this gem is not without its flaws as, since the "Great Eruption" which formed the Homunculus nebula and the more recent eruption which formed the Little Homunculus (Ishibashi et al. 2003), η Car has been enshrouded by a dusty cocoon which complicates observations in the UV and optical. Fortunately, η Car is extremely bright at X-ray wavelengths which suffer less from extinction, thus providing an invaluable probe of the inner nebula.

The exceptional monitoring of η Car at X-ray wavelengths (Corcoran et al. 2001, 2004; Corcoran 2005; Corcoran et al. 2010; Hamaguchi et al. 2007; Henley et al. 2008; Leyder et al. 2008, 2010; Pian et al. 2009) has characterised the periodic variability as indicative of a highly eccentric ($e \simeq 0.9$), long-period ($\sim$ 5.54 yr) binary system (Table 1). The binary hypothesis appears to be well supported by theoretical models (Pittard et al. 1998; Ishibashi et al. 1999; Pittard & Corcoran 2002; Akashi et al. 2006; Henley et al. 2008; Okazaki et al. 2008; Parkin et al. 2009; Kashi & Soker 2009b), as well as by observations at infrared (Whitelock et al. 1994, 2004; Nielsen et al. 2009), radio (Duncan & White 2003; Abraham et al. 2005b), optical (Damineli 1996; Damineli et al. 2000, 2008a,b; van Genderen et al. 2003; Nielsen et al. 2007), far ultra-violet (Iping et al. 2005), and $\gamma-$ray wavelengths (Tavani et al. 2009; Walter et al. 2010, - although see Ohm et al. 2010 and Abdo et al. 2010). In this scenario the X-ray emission originates from the shock heated plasma generated by the fast wind of a companion star which ploughs into the slow dense wind of η Car [1] (e.g. Pittard et al. 1998).

The observed X-ray lightcurve displays the general characteristics expected from a high orbital eccentricity colliding winds binary, but has some puzzling features. For instance, the most recent X-ray minimum was considerably shorter than the extended minima observed in previous cycles (Corcoran et al. 2001; Corcoran 2005;

parkin@mso.anu.edu.au

[1] For the remainder of this paper we refer to the larger star (commonly referred to as a luminous blue variable (LBV) star - although see Mehner et al. 2010a) and the smaller companion star (estimated to be of early O type or a WR star - Pittard & Corcoran 2002; Verner et al. 2005; Teodoro et al. 2008; Mehner et al. 2010a) as the primary and companion star, respectively.

Corcoran et al. 2010). The exact cause of the X-ray minimum is a matter of debate (for an overview of some of the possibilities see Parkin et al. 2009), yet it is now clear that models must also be able to account for the observed cycle-to-cycle variation.

The nature of the wind-wind collision region (WCR) has recently been investigated with 3D models. Using a Smoothed-Particle Hydrodynamics (SPH) model of the wind-wind collision, Okazaki et al. (2008) found that they could match the extended X-ray minimum. In contrast, adopting the 3D dynamical model of Parkin & Pittard (2008), Parkin et al. (2009) showed that when the spatial extent of the X-ray emission region and energy dependence of the emission and absorption were taken into consideration, the width of the observed X-ray minimum could not be reproduced by an eclipse of the X-ray emitting plasma alone. Furthermore, models with the preshock stellar winds at terminal velocity over-predicted the observed X-ray emission in the 7-10 keV band by an order of magnitude, indicating that a reduction in the preshock speed of the companion star's wind is required.

Such a reduction is plausible, as the highly eccentric orbit causes the WCR to enter into the wind acceleration region of the companion star around periastron passage. Considering the immense luminosity of the primary star, the acceleration of the companion's wind may also be significantly inhibited. A reduction in the preshock velocity will cause radiative cooling to become increasingly important in the postshock companion's wind, and will affect the stability of the WCR (Davidson 2002; Parkin et al. 2009). In fact, a ram pressure balance between the stellar winds may be lost and the shock may collapse onto the companion star (Parkin et al. 2009). In this case the 7-10 keV flux which originates predominantly from the apex of the WCR would be quenched, a feature which is necessary in models aiming to explain the extended X-ray minimum. However, it is unclear why a collapse of the WCR (if one occured) would be of a much shorter duration in the most recent periastron passage whilst being extended in previous cycles.

In this paper we describe our results from a suite of three dimensional (3D) simulations in which we have implemented radiative driving, gravity, orbital motion, and optically thin radiative cooling, allowing the rôle of wind acceleration, interacting radiation fields, and instabilities in the wind-wind collision region (WCR) on the gas dynamics and resulting X-ray emission to be explored. We first present simulations with static stars at a separation corresponding to periastron passage. The turbulent, highly unstable nature of the wind-wind collision region (WCR) is revealed, and results show that when the acceleration regions of the stars are considered the conditions in the postshock gas permit the growth of powerful non-linear thin-shell instabilities (NTSI - Vishniac 1994). Subsequent vigorous oscillations lead to the collision of dense fragments of the WCR against the companion star. Importantly, the 7-10 keV X-ray luminosity shows a marked reduction when compared to an equivalent simulation which neglects the wind acceleration. We then perform large-scale, high resolution simulations which include the orbital motion of the stars, and find that the rapid orbital motion of the stars around periastron acts to: reduce the degree of radiative inhibition of the preshock companion star's wind. Consequently, the catastrophic disruption of the WCR seen in the static stars simulation is not reproduced.

TABLE 1
Adopted system parameters for η Car.

Parameter	Value	Reference
Orbital period (d)	2024	1
Eccentricity (e)	0.9	1
a (au)	16.64	2
$d_{\rm sep}(\phi = 0.0)$ (10^{13} cm)	2.48	–
$d_{\rm sep}(\phi = 0.5)$ (10^{13} cm)	47.3	–
Distance (kpc)	2.3	3
ISM + nebula column (10^{22}cm^{-2})	5	4

Note. — a is the semi-major axis of the orbit and $d_{\rm sep}(\phi)$ is the binary separation as a function of orbital phase. References are as follows: 1 = Damineli et al. (2008b), 2 = Hillier et al. (2001), 3 = Davidson & Humphreys (1997), 4 = Hamaguchi et al. (2007).

We conclude that the behaviour of the observed X-ray emission from η Car around periastron is tied to the rate of radiative cooling in the postshock companion's wind. The suppression of the preshock companion's wind by radiative inhibition (albeit with a stronger radiation-wind coupling than explored in this work) could be an important trigger for rapid cooling. Furthermore, the differences between the observed short and long duration X-ray minima may be due to the companion's postshock gas conditions lying close to the dividing line between instability growth which merely perturbs the WCR, and far more vigorous NTSIs which destroy it (possibly causing the WCR to collapse onto the companion star in the process). The latter case may explain the longer observed minima.

The remainder of this paper is structured as follows: a description of the hydrodynamic model and the X-ray emission calculations are given in § 2. In § 3 we review some theoretical background relevant to our current investigation. The results of the hydrodynamic simulations are presented in § 4 (static stars at periastron separation), and § 5 (large-scale orbit). A discussion and suggestions for future directions are given in § 6, and we close with our conclusions in § 7.

2. THE MODEL

2.1. *Hydrodynamic modelling*

The wind-wind collision is modelled by numerically solving the time-dependent equations of Eulerian hydrodynamics in a 3D Cartesian coordinate system. The relevant equations for mass, momentum, and energy conservation are:

$$\frac{\partial \rho}{\partial t} + \nabla \cdot \rho \mathbf{v} = 0, \tag{1}$$

$$\frac{\partial \rho \mathbf{v}}{\partial t} + \nabla \cdot \rho \mathbf{v}\mathbf{v} + \nabla P = \rho \mathbf{f}, \tag{2}$$

$$\frac{\partial \rho E}{\partial t} + \nabla \cdot [(\rho E + P)\mathbf{v}] = \left(\frac{\rho}{m_{\rm H}}\right)^2 \Lambda(T) + \rho \mathbf{f} \cdot \mathbf{v}. \tag{3}$$

Here $E = \epsilon + \frac{1}{2}|\mathbf{v}|^2$, is the total gas energy, ϵ is the specific internal energy, $\mathbf{v}$ is the gas velocity, ρ is the mass density, P is the pressure, T is the temperature, and $m_{\rm H}$ is the mass of hydrogen. $\mathbf{f}$ is the force per unit mass and includes gravity and radiative driving terms.

We use the ideal gas equation of state, $P = (\gamma - 1)\rho\epsilon$, where the adiabatic index $\gamma = 5/3$.

The radiative cooling term, $\Lambda(T)$, is calculated from the MEKAL thermal plasma code (Mewe et al. 1995; Kaastra 1992) distributed in XSPEC (v11.2.0). The temperature of the unshocked winds is assumed to be maintained at $\approx 10^4$ K via photoionization heating by the stars. Throughout this work solar abundances are assumed (Anders & Grevesse 1989).

The body forces acting on each hydrodynamic cell are the vector summation of gravitational forces from each star, and continuum and line driving forces from the stellar radiation fields. The computation of the line acceleration is based on a local Sobolev (1960) treatment of the line transport, following the standard Castor, Abbott, & Klein (1975) (hereafter CAK) formalism developed for single OB star winds. To account for the correction to the line force due to the finite size of the stellar disk (i.e. the finite disk correction factor - Castor 1974; Pauldrach et al. 1986) we follow Cranmer & Owocki (1995) and define a "wind centred" coordinate system (x', y', z') to calculate the local velocity gradient (see Fig. 1) and then move to the "star centred" coordinate system (x, y, z) to determine the projected velocity gradient along the direction vector $\hat{\mathbf{n}}$ using the following transformation,

$$\begin{aligned} x &= (x' \cos\theta_0 + z' \sin\theta_0)\cos\phi_0 - y' \sin\phi_0 \\ y &= y' \cos\phi_0 + (x' \cos\theta_0 + z' \sin\theta_0)\sin\phi_0 \\ z &= z' \cos\theta_0 - x' \sin\theta_0 \end{aligned} \qquad (4)$$

The vector radiative force per unit mass, $\mathbf{g}_{\rm rad}$, is then computed from a numerical Gaussian integration (using 8 directional vectors) of the intensity $I(\hat{\mathbf{n}})$ times $\hat{\mathbf{n}} \cdot \nabla(\hat{\mathbf{n}} \cdot v)$ over the solid angle covering the stellar disk,

$$\mathbf{g}_{\rm rad} = \frac{\sigma_c^{1-\alpha} k}{c} \oint I(\hat{\mathbf{n}}) \left[\frac{\hat{\mathbf{n}} \cdot \nabla(\hat{\mathbf{n}} \cdot v)}{\rho v_{\rm th}} \right]^{\alpha} \hat{\mathbf{n}} d\mathbf{\Omega}. \qquad (5)$$

α and k are the standard CAK parameters, $\sigma_{\rm e}$ is the specific electron opacity due to Thomson scattering, and $v_{\rm th}$ is a fiducial thermal velocity calculated for hydrogen. Shadowing by the companion star is accounted for in our calculations, and in such cases only the visible part of the stellar disk contributes to the radiative driving force. The line driving is set to zero in cells with temperatures above 10^6 K, since this plasma is mostly ionized. Further details concerning the line force calculations can be found in Cranmer & Owocki (1995) and Gayley et al. (1997).

The stellar winds are initiated in the instantaneously accelerated and radiatively driven stellar winds simulations in two slightly different ways. In the former, appropriate hydrodynamic variables (i.e. $\rho, P, \mathbf{v}$) are mapped into cells residing within a radial distance $R_{\rm map}$ which is a function of stellar separation (see Appendix A). Thus,

$$\rho_{\rm i} = \frac{\dot{M}_{\rm i}}{4\pi r_{\rm i}^2 |v_{\infty {\rm i}}|}, \qquad (6)$$

where $r_{\rm i}$ is the distance of the cell from the respective star and the subscript i refers to the wind being considered. In contrast, to initiate radiatively driven stellar winds we map hydrodynamic variables determined from single star wind profiles (calculated with the parameters noted in Table 2) within a stellar radius of $\simeq 1.1\ R_*$ after every time step. As noted by Pittard (2009), it is necessary to resolve the region above the stellar surface (i.e 0.1 R_*) with at least 3 cells. To distinguish between the stellar winds in the simulations we include an advected scalar variable in the hydrodynamics calculations.

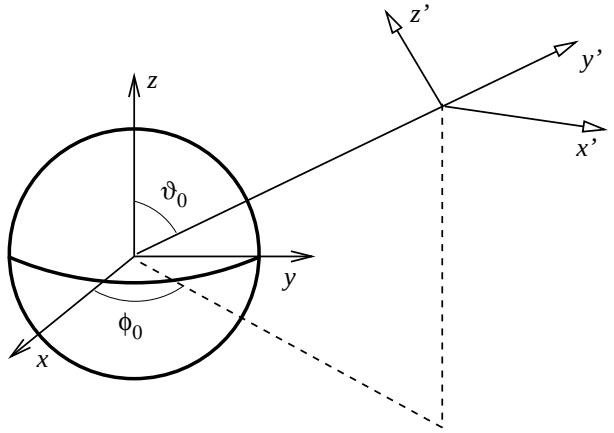

FIG. 1.— Schematic diagram illustrating the transformation from the "wind centred" to the "star centred' coordinate system.

It should be noted that the primary is an LBV, and therefore it is unclear to what level using the CAK formalism is appropriate to describe the wind driving from this star. Furthermore, Smith et al. (2003) inferred a higher rate of mass-loss at the poles based on the observation of varying absorption as a function of latitude in the reflected emission from the Homunculus nebula, which may be related to the rotation rate of the primary star, though it may also be related to the presence of the companion star (Groh et al. 2010a). Since we do not consider a latitude dependence, the mass-loss rates which we infer are likely indicative of the equatorial wind (assuming the equatorial and orbital planes are aligned).

Adopting solar abundances may also affect the inferred mass-loss rates. For instance, Hillier et al. (2001) found N to be significantly enhanced, while C and O could be as low as 1/25 and 1/50 solar, respectively. Although these differences will alter the opacity of the primary wind, we do not anticipate that the observed X-ray spectrum at $E > 1$ keV will be significantly affected.

2.2. *The hydrodynamic code*

The simulations presented in this work were performed using version 3.1.1 of the FLASH (Fryxell et al. 2000; Dubey et al. 2009) hydrodynamical code. This code operates with a block-structured AMR grid (e.g. Berger & Oliger 1989) using the PARAMESH package (MacNeice et al. 2000) under the message-passing interface (MPI) architecture. The piecewise-parabolic method of Colella & Woodward (1984) is used to solve the hydrodynamic equations. Customized units have been implemented into the FLASH code for radiative cooling for optically-thin plasma using the explicit method described by Strickland & Blondin (1995), radiative driving, gravity, and orbital motion. Simulations are performed with the stars fixed at periastron (§ 4) and as they move through an orbit (§ 5), and a description of the grids used can be found in the relevant section (i.e. size, shape, resolution, and refinement criteria).

We note that as a goal of our investigation is to ex-

TABLE 2
Parameters used to calculate the line driving of the stellar winds.

Parameter	Primary	Secondary	Reference
M ($\mathrm{M}_\odot$)	120	30	1
R_* ($\mathrm{R}_\odot$)	100	20	2
$T_{\rm cs}$ (K)	25,800	30,000	3
L_* ($10^6\mathrm{L}_\odot$)	4	0.3	3
k	0.30	0.50	–
α	0.52	0.68	–
$\dot{M}$ ($\mathrm{M}_\odot\,\mathrm{yr}^{-1}$)	4.8×10^{-4}	1.4×10^{-5}	3
v_∞ ($\mathrm{km\,s}^{-1}$)	500	3000	4
η	0.18		–

Note. — M is the stellar mass, R_* is taken to be the radius of the gravitationally bound core of the star (which for the primary star is taken to be at a radius of $100\,\mathrm{R}_\odot$, i.e. the photosphere will exist somewhere in the stellar wind), $T_{\rm cs}$ is the temperature at R_*, L_* is the stellar luminosity, $\dot{M}$ is the stellar mass-loss rate, v_∞ is the wind terminal velocity, and $\eta = \dot{M}_2 v_{\infty 2}/\dot{M}_1 v_{\infty 1}$ is the wind momentum ratio. k and α are the CAK line driving parameters, where subscripts 1 and 2 are used to define the coupling between the winds and the radiation fields of the primary and secondary star respectively. Note that single star mCAK calculations (Pauldrach et al. 1986) were performed to determine values of k and α required to produce the desired $\dot{M}$ and v_∞ for each wind. References are as follows: 1 = Hillier et al. (2001), 2 = Corcoran & Hamaguchi (2007), 3 = Parkin et al. (2009), 4 = Pittard & Corcoran (2002).

plore the rôle of instabilities in the WCR, a grid-based hydrodynamic code is advantageous for this purpose in comparison to an SPH code (Agertz et al. 2007).

2.3. *X-ray emission*

To calculate the X-ray emission from the simulation we use emissivities for optically thin gas in collisional ionization equilibrium obtained from look-up tables calculated from the MEKAL plasma code containing 200 logarithmically spaced energy bins in the range 0.1-10 keV, and 101 logarithmically spaced temperature bins in the range $10^4 - 10^9$ K. When calculating the emergent flux we use energy dependent opacities calculated with version C 08.00 of Cloudy (Ferland 2000, see also Ferland et al. 1998). The advected scalar is used to separate the X-ray emission contributions from each wind.

Based on the findings of Parkin & Pittard (2010), we note that *numerical* heat conduction from the hot, low density postshock companion star wind to the cooler, higher density postshock gas of the primary star's wind will occur in the simulations. This effect is purely numerical in origin, and one must be careful when interpreting the derived X-ray emission. Therefore, as a cautionary measure we only consider the X-ray emission contributed by the postshock companion star's wind.

3. THEORETICAL BACKGROUND OF RADIATIVELY DRIVEN WINDS

3.1. *Radiatively driven winds of single hot stars*

For the stellar atmosphere to be driven by the radiation field there is the simple requirement that $GM/r^2 < g_{\rm rad}$. The key to accurately describing the motion of the wind comes in the form of the $g_{\rm rad}$ term, and significant progress has been made using the force multiplier, $\mathfrak{M}(t) = kt^{-\alpha}$, originally proposed by CAK,

$$g_{\rm rad} = \frac{\sigma_e F k t^{-\alpha}}{c}, \tag{7}$$

where F is the radiative flux, and $t = \sigma_{\rm e} v_{\rm th} \rho [\hat{\mathbf{n}} \cdot \nabla (\hat{\mathbf{n}} \cdot v)]^{-1}$ is the Sobolev optical depth parameter. The force multiplier parameters α and k are determined from a power law fit to $\mathfrak{M}(t)$. k can be interpreted as the fraction of flux that would be blocked if all lines were optically thick. α is the ratio of the line acceleration from optically thick lines to the total one.

3.2. *Finite disk correction factor*

A simplifying assumption adopted in early works on radiatively driven winds (e.g. Lucy & Solomon 1970; CAK) was that of radially streaming photons, i.e. a point source of radiation. In this case the projected velocity gradient becomes $\partial v_{\rm r}/\partial r$ where $v_{\rm r}$ is the radial velocity, and angle integrals simplify to purely radial terms. Unfortunately, the assumption of radially streaming photons is a poor one close to the star where the wind is rapidly accelerated. To circumvent this problem it has become common place to incorporate a multiplicative factor to correct for the finite size of the stellar disk, K, which is attained by adopting the exact optical depth rather than the radial one,

$$K(r, v, dv/dr) \equiv \frac{\mathbf{g}_{\rm rad}(\text{finite disk})}{\mathbf{g}_{\rm rad}(\text{point source})} \tag{8}$$

$$= \frac{(1+\sigma)^{1+\alpha} - (1+\sigma\mu_*^2)^{1+\alpha}}{\sigma(1+\alpha)(1+\sigma)^\alpha(1-\mu_*^2)} \tag{9}$$

where θ is the angle subtended between the radial direction and a point on the stellar disk, $\mu = \cos\theta$, $\mu_* = \sqrt{1-(R_*/r)^2}$, and $\sigma = (d\ln v/d\ln r) - 1$ (Castor 1970). K is commonly referred to as the *finite disk correction factor* (FDCF) (Castor 1974; CAK; Pauldrach et al. 1986). $\mathfrak{M}(t)_{\rm FDCF}$ is related to the standard (under the assumption of radially streaming photons) force multiplier, $\mathfrak{M}(t)$, via,

$$\mathfrak{M}(t)_{\rm FDCF} = K\mathfrak{M}(t) \tag{10}$$

In certain instances (e.g. Pauldrach et al. 1986; Stevens & Pollock 1994) the FDCF is approximated as a purely radial, monotonic function (i.e. $K(r, v, dv/dr) \sim K(r)$). Fig. 2 shows a comparison of monatonic and dynamically consistent FDCFs; a monotonic FDCF always stays below 1, whereas a dynamically consistent FDCF rises above 1 in the wind acceleration region. For comparison we have also plotted the numerical evaluation of the FDCF which we have implemented into FLASH - there is a good agreement with the analytical result.

3.3. *Interacting radiation fields in binary systems*

In the standard CAK model for radiatively driven winds the outwards acceleration is produced by the radiation field of the star. If one introduces an opposing radiation field two effects become apparent: radiative inhibition (Stevens & Pollock 1994) and radiative braking (Gayley et al. 1997 - see also Owocki & Gayley 1995). The former refers to the reduction of the net rate of acceleration of a stellar wind due to the opposing radiation field, whereas the latter refers to the (sudden) deceleration of a stellar wind before it reaches the WCR. In the Stevens & Pollock (1994) formulation of radiative inhibition, the basic premise is that the line force (Eq. 7)

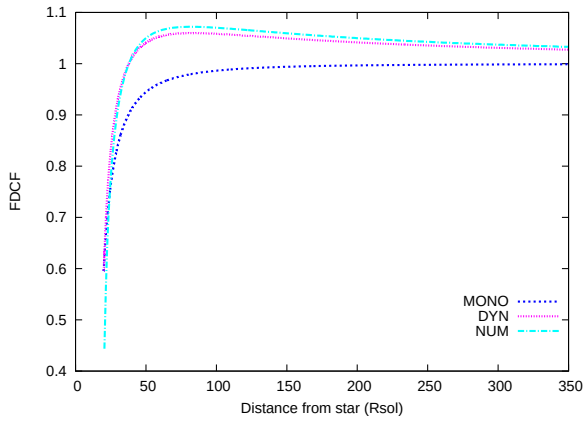

FIG. 2.— Comparison of finite disc correction factors (FCDFs) calculated assuming monotonic flow (MONO, e.g. Stevens & Pollock 1994), with dynamical consistence (DYN, i.e. including velocity gradient terms - see Eq. 9), and via a numerical evaluation (NUM - see § 2.1). The FDCFs are calculated using the companion (single) star wind velocity profile (see Fig. 3).

becomes

$$g_{\rm rad} = \frac{\sigma_{\rm e}\mathfrak{M}(t)}{c}\{F_1K_1 - F_2K_2\} \qquad (11)$$

where F_1, F_2 are the radiative fluxes, and K_1, K_2 are the finite disk correction factors for stars 1 and 2, respectively. The radiative inhibition calculations presented by Stevens & Pollock (1994) adopted a monotonic FDCF and, as noted by Gayley et al. (1997), it was for this reason that they did not see radiative braking in their calculations.

Radiative inhibition is expected to be important if the stars are close enough that their opposing radiation fields reduce the net force within the acceleration region of the winds, whereas radiative braking is important in systems where the imbalance in wind momenta is such that the stronger wind approaches the companion star close enough for its radiation pressure to exceed the wind ram pressure. Depending on the stellar and system parameters adopted both effects may be important for η Car (Parkin et al. 2009).

3.4. *Considerations for* η Car

The binary orbit of η Car is highly eccentric. Therefore, for a large part of the orbit the stars are well separated, the winds have accelerated to terminal velocity when they reach the WCR, and the effects of radiative inhibition and radiative braking are negligible. However, an accurate description of wind acceleration (particularly of the companion's wind) is essential around periastron when the WCR enters into the wind acceleration regions.

Compared to a monotonic FDCF, a dynamically consistent FDCF will provide additional acceleration close to the star driving the wind (see § 3.2). Therefore, one may wonder what difference using dynamically consistent FDCFs in Eq. 11 has on the level of radiative inhibition? In Fig. 3 we show the results from static two-star radiative driving calculations for η Car at periastron. Using a monotonic FDCF and with $k_1 = k_2$ and $\alpha_1 = \alpha_2$ (i.e. the coupling between the primary's radiation and the companion's wind uses $k = 0.50$ and $\alpha = 0.68$) we see that the terminal velocity attained by the companion star wind is dramatically reduced from 3000 km s^{-1} (without RI) to $\simeq$ 1500 km s^{-1} (RI - mono FDCF). If we include a dynamically consistent FDCF the level of radiative inhibition is lessened and the maximum velocity attained now increases to $\simeq$ 1600 km s^{-1} (RI - dynm FDCF). Interestingly, the velocity profile now displays radiative braking. Comparing the radiative driving calculations against those from a numerical hydrodynamic simulation calculated using the code described in § 2.1 (HS), we see good agreement, albeit with a minor difference in the position of the braking radius (the radius at which rapid deceleration of the wind occurs).

In both the radiative inhibition (Stevens & Pollock 1994) and braking (Owocki & Gayley 1995; Gayley et al. 1997) theories the line force is assumed to take the form of Eq. 11, and in so doing the force multiplier parameters used to accelerate/decelerate the stellar wind are assumed to be equivalent (i.e. $k_1 = k_2$ and $\alpha_1 = \alpha_2$ within the wind of star 1). At the alternative extreme, the line force could be described as[2]

$$g_{\rm rad} = \frac{\sigma_{\rm e}}{c}\{\mathfrak{M}_1(t)F_1K_1 - \mathfrak{M}_2(t)F_2K_2\} \qquad (12)$$

where $\mathfrak{M}_{\rm w}(t) = k_{\rm w}t^{-\alpha_{\rm w}}$ and the subscript w denotes the wind which the line driving parameters are describing. Fig. 3 shows the result of a hydrodynamic calculation (with radiatively driven winds) where $g_{\rm rad}$ is equivalent to that of Eq. 12 (i.e. the coupling between the primary's radiation and the companion's wind uses $k = 0.30$ and $\alpha = 0.52$). The resulting level of radiative inhibition is lower and the companion's wind reaches a maximum velocity of 2200 km s^{-1} (HS - $k_1 = k_2$, $\alpha_1 = \alpha_2$). Furthermore, the braking radius has increased by a factor of ~ 2. The explanation for this can be found by considering the line driving parameters of each individual wind. The significantly higher luminosity of the primary star means that to achieve its huge mass-loss rate we actually require lower values of k and α than the companion star (with its lower luminosity) requires to drive a weaker wind. In essence, the coupling between the primary's radiation field and its wind is weaker than the respective case for the companion star. Therefore, if the primary's radiation field is more strongly coupled to the companion's wind (i.e $k_1 = k_2$ and $\alpha_1 = \alpha_2$), the decelerating force, and thus the net level of radiative inhibition, will be greater. Clearly, this result has implications for the dynamics of the WCR, and the influence of radiative inhibition on the X-ray emission from η Car (Parkin et al. 2009). In the following work we conservatively adopt the assumption of weaker coupling (Eq. 12), but note that it could be stronger in reality. If this were the case one would expect lower preshock velocities for the companion's wind, and reduced X-ray emission, particularly at higher energies (e.g. $E > 2$ keV).

4. PERIASTRON SIMULATIONS

As the stars move towards periastron passage their separation contracts, their orbital velocities increase, and

[2] It is currently unclear what the correct choice for the coupling between the radiation field of a star with the opposing star's wind is. We merely note that previous works on the interaction of radiation fields in binary star systems (e.g. Pittard et al. 1998; Gayley et al. 1997; St-Louis et al. 2005; Parkin et al. 2009) suggest that the actual coupling lies somewhere between the two cases presented in Eqs. 11 and 12.

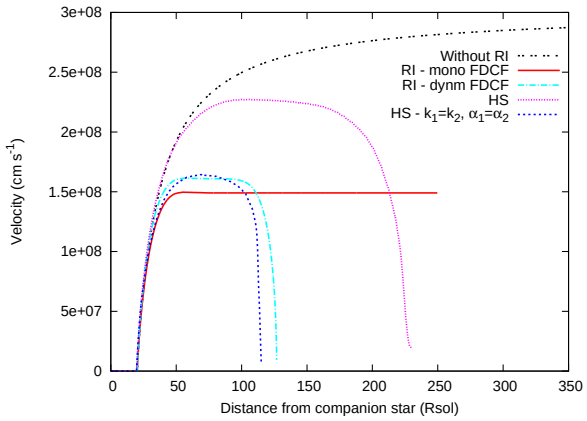

FIG. 3.— Companion star wind velocity along the line of centres between the stars. The primary star is situated at a distance of $359\,R_\odot$ (corresponding to periastron separation when $e = 0.9$). The following solutions are shown: without radiative inhibition (RI)(i.e. single star), RI using a monotic FDCF, RI using a dynamically consistent FDCF, and a numerical hydrodynamic simulation (HS) with separate CAK parameters for each wind, and a HS but with k_1 and α_1 used to drive both winds. The stellar and line driving parameters used to perform these calculations are noted in Table 2.

the preshock and postshock gas density (and velocity in the accelerating winds case) undergo a considerable rate of change as the WCR moves closer to the stars. To form a basis for qualitative and quantitative predictions for the large-scale simulations that will follow (§ 5), we begin with simulations focused on periastron passage where orbital motion is not included. A fixed resolution grid with cell size of $\simeq 9.8 \times 10^{10}$ cm is used (i.e. no AMR) and the simulation box extends from $x = z = \pm 2.34 \times 10^{12}$ cm and $y = 0 - 1.88 \times 10^{13}$ cm (corresponding to $x \times y \times z = 32 \times 192 \times 32$ cells). The companion star is situated at $(x, y, z) = (0,0,0)$ and the primary star is situated at $(x, y, z) = (0, 2.5 \times 10^{13}$ cm, $0)$. Zero-gradient boundary conditions are used on all faces of the simulation box. The calculations were evolved for a time of 4×10^6 s, corresponding to $\simeq 0.02$ in orbital phase, and therefore sufficiently long to examine the growth of instabilities over the characteristic time that the stars spend at closest approach. For comparison we have performed simulations with instantaneously accelerated winds (model Peri-IA) and radiatively driven winds (model Peri-RD). We now proceed with a discussion of the results of these models, including calculations of the intrinsic 7-10 keV X-ray luminosity and its variability, and also the results of additional tests performed with varying grid resolutions and at separations corresponding to orbital phases around periastron.

The periastron simulations are initialized with two opposing flows separated by a contact discontinuity at the ram pressure balance point between the winds. As model Peri-IA is evolved through time the winds collide and shocks are formed. The primary's relatively slow and dense wind cools rapidly to form a thin dense layer, whereas the faster, more tenuous wind of the companion star behaves quasi-adiabatically (Pittard et al. 1998; Pittard & Corcoran 2002; Parkin et al. 2009). Consequently, there is a large density and temperature contrast between gas on either side of the contact discontinuity and the growth of Rayleigh-Taylor (RT) instabili-

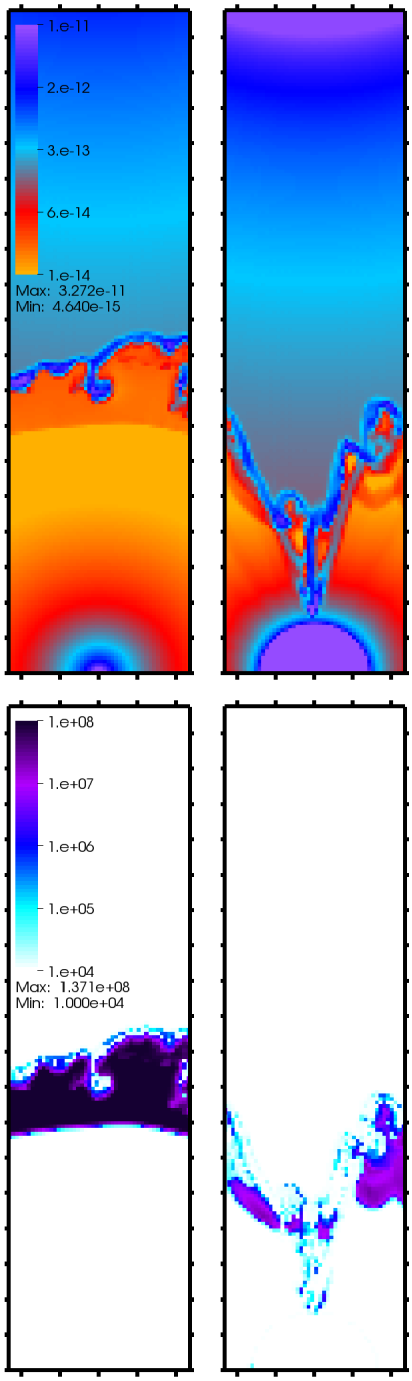

FIG. 4.— Density (upper row) and temperature (lower row) snapshots of the $x - y$ plane from models Peri-IA (left column) and Peri-RD (right column) at a simulation time of 2.4×10^6 s. The companion star is situated at the lower boundary and the primary star is situated beyond the opposite end of the box. All plots show a region of $x = \pm 2.34 \times 10^{12}$ cm and $y = (0 - 1.88 \times 10^{13}$)cm - tick marks correspond to a distance of 1×10^{12} cm. The hot postshock companion wind in model Peri-IA acts as a "cushion" against thin-shell instability. In contrast, NTSIs are permitted to grow by the lower temperature postshock companion's wind in model Peri-RD. A volume rendering of the model Peri-RD density distribution is shown in Fig. 5.

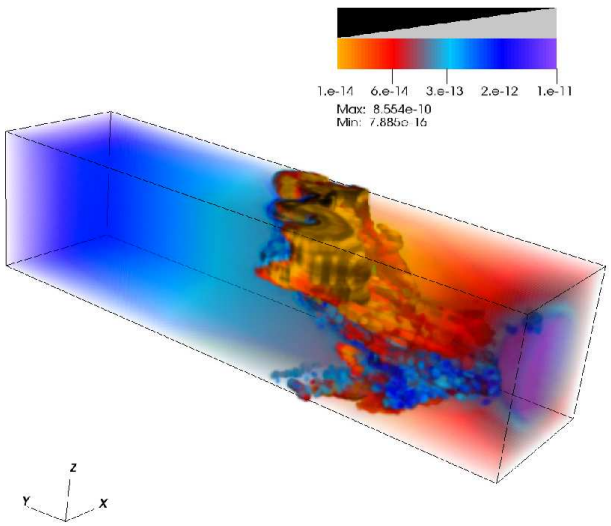

FIG. 5.— Density volume rendering of model Peri-RD at a simulation time of 2.4×10^6 s. The companion star is situated to the right of the image (the end face of the box cuts through its centre) and the primary star is situated beyond the opposite end of the box such that only a small area of its surface fits within the box. Driven by instabilities in the WCR, fragments of cold, dense postshock primary wind gas (blue) can be seen colliding against the companion star (purple).

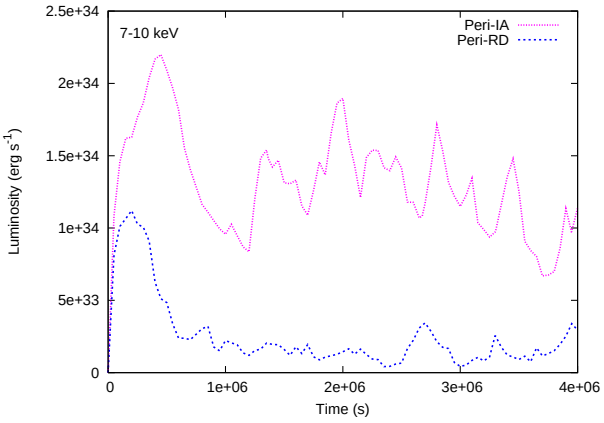

FIG. 6.— Variability of the intrinsic 7-10 keV X-ray luminosity for models Peri-IA and Peri-RD. Note that the simulation grid for models Peri-IA and Peri-RD is focused on the region between the stars, therefore the total X-ray emission from the entire WCR cannot be calculated. However, our comparison here highlights important differences between the flux levels of the two models.

ties ensues. Subsequent perturbations to the contact discontinuity seed the linear thin-shell instability (Vishniac 1983). However, the hot, quasi-adiabatic postshock companion's wind has a sufficiently fast sound speed, and thus rate of response to perturbations in the contact discontinuity by the dense thin layer, to render it linearly stable and the regime of non-linear instability growth is never reached (Vishniac 1994). Therefore, the thermal pressure of the hot postshock companion's wind acts like a cushion and prevents an instability-driven collapse/collision of the WCR against the companion star

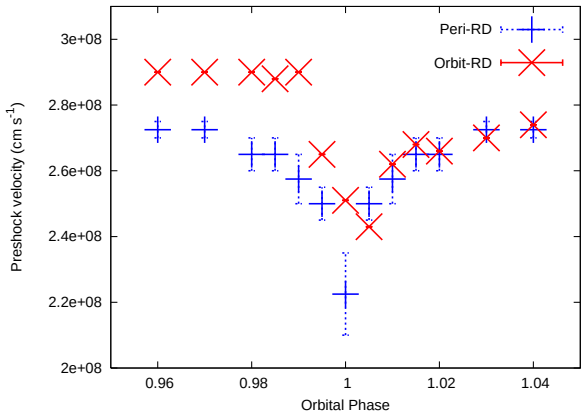

FIG. 7.— Preshock companion wind speed measured along the line of centres as a function of orbital phase for simulations Peri-RD and Orbit-RD.

(Fig. 4).

However, the inclusion of the radiative driving of the stellar winds in model Peri-RD, and thus of the wind acceleration regions, introduces some important differences to this picture. Firstly, by a simulation time of $t = 10^5$ s the primary's radiation field has reduced the preshock companion's wind velocity from $\simeq 2500$ km s^{-1} to $\simeq 2200$ km s^{-1}, and radiative inhibition of the initial (single star) velocity profile (see Fig. 3) is evident. As such, the postshock gas temperature is lower. Secondly, the WCR moves slightly closer to the companion star to attain a new ram pressure balance and in so doing the preshock (and thus postshock) gas densities are higher. The combination of these factors causes radiative cooling to become important for the postshock companion wind, and as the gas cools it loses the thermal pressure support which ensures its stability. When this occurs NTSIs begin to grow and by a simulation time of 7×10^5 s oscillations in the WCR push a dense clump of postshock primary wind towards the companion star. This clump then fragments from the WCR and passes deep into the companion's wind acceleration region, narrowly missing the star. Driven by the NTSI, the position of the WCR continues to oscillate throughout the simulation causing the mean preshock velocity of the companion's wind between the stars to vary in the range $\sim 2100 - 2350$ km s^{-1}. At a time of 2.4×10^6 s multiple fragmented clumps of postshock primary wind collide against the companion star (see Figs. 4 and 5). Such collisions occur at multiple times throughout the simulation, interspersed by brief recoveries as the shock oscillates away from the companion star.

An obvious question is why do collisions occur in model Peri-RD but not in model Peri-IA? As stated above, when radiative cooling becomes important for the postshock companion's wind in model Peri-RD linear thin-shell instabilities can grow non-linearly with devastating results for the WCR. Hence, we can quantify the difference between models Peri-RD and Peri-IA using the cooling parameter (Stevens et al. 1992)

$$\chi = \frac{t_{\rm cool}}{t_{\rm flow}} = \frac{v_8^4 d_{12}}{\dot{M}_{-7}}, \qquad (13)$$

where $t_{\rm cool}$ is the cooling time, $t_{\rm flow} = 10^{12} d_{12}/s_{\rm ps}$ is the

flow time, $s_{\rm ps}$ is the postshock sound speed along the line of centres, v_8 is the preshock gas velocity (in 10^8 cm s^{-1}), d_{12} is a characteristic distance (in 10^{12} cm), and $\dot{M}_{-7}$ is the mass-loss rate (in $10^{-7}\,{\rm M}_\odot\,{\rm yr}^{-1}$). Here we take d_{12} to be the distance of the companion shock from the star as we are interested in the importance of cooling close to the WCR apex. As a rule of thumb $\chi > 1$ indicates quasi-adiabatic gas whereas $\chi \lesssim 1$ indicates that gas cools rapidly. Examining χ for the companion's wind we find values of 3.6 and 1 for models Peri-IA and Peri-RD, respectively. Therefore, on the timescales that we are interested in (i.e. the closest approach of the stars around periastron passage) the differences in postshock gas conditions between models Peri-RD and Peri-IA are sufficient to trigger rapid radiative cooling and the subsequent growth of catastrophic instabilities in the former. Interestingly, the differences between postshock gas conditions in models Peri-RD and Peri-IA are relatively minor, but because of the strong dependence on the preshock velocity there is a fine line between a WCR which is only plagued by instabilities and one in which the instabilities ultimately destroy it. The differences in the X-ray minima (extended in 1998 and 2003.5 versus the quick recovery seen in 2009), may therefore reflect differences in the behaviour of the WCR caused by a small change in one or both winds. We note again that our adopted radiation-wind coupling essentially provides a lower limit to the degree of radiative inhibition of the companion's wind. If a stronger coupling were adopted the companion wind would collide at lower speeds and radiate more efficiently, and a WCR disruption (potentially even more ferocious) as in model Peri-RD would occur more readily.

Akashi & Soker (2010) have recently presented numerical simulations akin to model Peri-IA. However, while the radiation fields were ignored, the gravitational influence from *only* the companion star was included. This results in the balance point of the WCR shifting closer to the companion star, thereby increasing the cooling rate of the shocked gas from the companion's wind, and making it easier for instabilities in the WCR to strike the companion star. Clearly, one must include all relevant forces acting on the shocked gas.

4.1. *X-ray emission*

Previous models of energy dependent X-ray emission from η Car have revealed that if the preshock companion's wind is assumed to be at terminal velocity at orbital phases coinciding with the extended X-ray minimum there is an overestimate of roughly an order of magnitude in the 7-10 keV flux when compared to that observed by *XMM-Newton* (Parkin et al. 2009). To examine whether the differences between models Peri-IA and Peri-RD can provide clues to alleviating this discrepency we have performed X-ray calculations on the simulation output (Fig. 6). The X-ray luminosity rapidly rises as the winds start to collide in the simulation and then reaches a peak before declining. In model Peri-RD the first minimum corresponds to the first occurence of a fragment of dense postshock primary star wind coming into close proximity and/or colliding with the companion star. In contrast, no such collisions occur in model Peri-IA, and the variability in the 7-10 keV flux instead corresponds to oscillations in the shock front. The lower preshock velocities, and thus lower postshock gas temperatures (see Fig. 4), in model Peri-RD combined with the shock obliquity created by the NTSI results in an average intrinsic 7-10 keV luminosity which is roughly a factor of 8 lower than that calculated for model Peri-IA. Therefore, it seems that a substantial disruption of the WCR can provide a plausible explanation for the observed behaviour of the hard X-ray flux (Hamaguchi et al. 2007).

4.2. *Resolution dependence*

The growth rate of instabilities are dependent on the wavelength, with smaller wavelengths producing faster growth rates. To examine the dependence on grid resolution we have performed tests[3] with cell sizes of $(4.9-39.2)\times10^{10}$ cm. Encouragingly, the general characteristics appear consistent. In each case instabilities grow and break-up the WCR causing stochastic collisions between dense clumps and the companion star. There does not appear to be any correlation between the grid resolution and the frequency of collisions.

Additional tests were performed using simulations boxes with a cell size of $\simeq 9.8\times10^{10}$ cm and a width up to $x = z = \pm3.5\times10^{12}$ cm. Consistent with model Peri-RD, when the acceleration (and radiative inhibition) of the companion's wind are considered the WCR becomes disrupted. Furthermore, the significantly lower 7-10 keV X-ray flux illustrated by the comparison between models Peri-RD and Peri-IA is reproduced.

4.3. *Variation of preshock velocity with orbital phase*

The separation of the stars changes rapidly around periastron passage and, therefore, so does the level of radiative inhibition, and the preshock companion star wind velocity. To examine this orbital phase dependence we have repeated model Peri-RD with stellar separations corresponding to orbital phases in the range $\phi = 0.96 - 1.04$, the results of which are plotted in Fig. 7. Error bars have been included to indicate the range of preshock velocities attained due to oscillations in the position of the companion shock. As the stellar separation tends towards its periastron value the instabilities become more vigorous, perturbing the shock front in the wind acceleration region (where the velocity gradient is high) and thus broadening the range of sampled velocities.

Comparing Fig. 7 against figure 21 of Parkin et al. (2009) it is evident that the conservative assumption of weak coupling adapted in the present paper leads to a reduced level of radiative inhibition and noticeably higher preshock velocities (even though fragments of the WCR stochastically collide with the companion star at $\phi = 1.0$ an average preshock velocity of $\simeq$ 2200 km s^{-1} is attained)[4].

[3] Note that to accurately model the acceleration of the stellar wind requires that the resolution not decrease in regions of sharp velocity gradient (i.e. within a radius of $\sim 3\ R_*$). Hence in the resolution tests the companion star wind acceleration region is covered with cells of side $\lesssim 9.8\times10^{10}$ cm and we only vary the cell size for *postshock* gas using the AMR capability of the code.

[4] In this work the winds are initiated by forcing an outflow in a spherical shell around each star. This prevents accretion from overpowering the wind, which may shut down the companion's wind for a significant period of time (Soker 2005; Akashi et al. 2006; Kashi & Soker 2009a)

5. ORBIT SIMULATIONS

While the periastron simulations presented in § 4 provide some interesting insight, to fully understand the flow dynamics and resulting X-ray emission from η Car we must perform simulations which include the motion of the stars. For this purpose we have performed two large-scale simulations: one in which the winds are assumed to be instantaneously accelerated at the surface of the star (model Orbit-IA), and another where the winds are radiatively driven (model Orbit-RD). Our adopted orbital and stellar parameters are noted in Tables 1 and 2. The mapping of the winds in model Orbit-IA is described in Appendix A.

To model the orbit of the η Car binary system we use a simulation domain which extends from $x = y = \pm 2 \times 10^{15}$ cm and $z = (0 - 2 \times 10^{15})$cm. Outflow boundary conditions are used for all faces of the simulation box except the lower z boundary which is a symmetry boundary. The grid is initialized with $x \times y \times z = 16 \times 16 \times 8$ cubic blocks each containing 8^3 cells. We allow for 9 levels of refinement, which results in an effective resolution on the finest grid level of $x \times y \times z = 32768 \times 32768 \times 16384$ (i.e. a cell size of 1.22×10^{11} cm or 1.75 $R_\odot$). The refinement of the grid is determined using a second-derivation error check (Fryxell et al. 2000) on ρ and the requirement of an effective number of cells between the stars to accurately describe the WCR dynamics (see Appendix B). The former identifies cells for refinement (and derefinement), whereas the latter controls the maximum resolution (for postshock gas) at a given orbital phase.

In the following we discuss the dynamics from simulations Orbit-IA and Orbit-RD, focusing first on the large-scale dynamics and then concentrating on the occurrences around periastron passage. We then present the results of X-ray calculations performed on the simulation output and detailed comparisons against observed lightcurves and spectra obtained with *RXTE* and *XMM-Newton*.

5.1. *Dynamics*

5.1.1. *Large-scale dynamics*

For most of the orbit the stars advance relatively slowly and the effects of orbital motion on the gas dynamics are modest. At these times the separation of the stars is sufficiently large for the stellar winds to be at terminal velocity when they reach their respective shock. However, around periastron passage the orbital velocities and stellar separation change rapidly as the stars career past each other. The rapid motion of the stars around periastron passage acts to contort the WCR into a spiral-like shape which subsequently expands outwards with the flow (Okazaki et al. 2008; Parkin et al. 2009). Figs. 8 and 9 show a series of gas density and temperature snapshots from simulations Orbit-IA and Orbit-RD, respectively, from which the salient features of the wind-wind collision and the effects of orbital motion can be seen. The contact discontinuity separates the winds, being abutted by a thin dense layer of postshock primary wind on one side, and a thicker "puffed-up" region of high temperature quasi-adiabatic postshock companion wind on the other. The density contrast and velocity shear across the contact discontinuity subject it to Kelvin-Helmholtz (KH) and RT instabilities.

At $\phi = 0.5$, the stars are at their largest separation, moving at their slowest orbital velocities, and it is apparent that a reasonable approximation to the X-ray emitting part of the WCR can be attained from a 2D model which neglects orbital motion (Pittard & Corcoran 2002). The apex of the WCR is closer to the primary star in model Orbit-RD than in model Orbit-IA due to the primary's wind ram pressure being slightly lower at an equivalent radius in the former - this is a numerical artifact resulting from the different ways by which the winds are initiated in the models. By $\phi = 0.9$ the stars have moved around in their orbits and their separation has reduced, yet the general shape of the large scale WCR has not changed considerably. However, the rapid motion of the stars during a brief period around periastron causes the WCR close to the stars to become very distorted (see Figs. 12 and 13), although the large scale WCR is not impacted upon by periastron passage at $\phi = 1.0$. At $\phi = 1.1$ the contortion of the WCR has had time to advect out in the flow, and the spiral structure of the WCR visible in previous 3D models is reproduced (Okazaki et al. 2008; Parkin et al. 2009). Interestingly, the increasing influence of orbital motion as the stars approach periastron results in an increasingly asymmetric temperature distribution in the postshock gas, with gas in the leading arm of the WCR clearly at a higher temperature than gas in the trailing arm (Figs. 8 and 9). In model Orbit-IA the postshock gas in the trailing arm is far from smooth; there are thin, dense filaments separated by low density, rarefied gas.

Fig. 10 displays a snapshot of the 3D structure of the WCR at periastron in simulation Orbit-RD. The clumpy/rippled texture to the WCR is clearly evident, as is the immense difference in scale between the large scale structure of the WCR and the region between the stars where the most ferocious activity occurs.

The snapshots of simulations Orbit-IA and Orbit-RD in Figs. 8 and 9 reveal a number of noticeable differences. Firstly, the opening angles of the primary star and companion star shocks are slightly larger in model Orbit-RD when compared to model Orbit-IA. This occurs due to the radiation fields of the stars; off-axis the preshock speed is greater than the on-axis preshock speed. The radiation fields of the stars also cause differences in the postshock gas between the two simulations. For instance, there are less instabilities in the WCR in model Orbit-RD when compared to model Orbit-IA. Examining the layer of postshock primary wind in the two models we find that the gas velocity (density) is higher (lower) in model Orbit-RD. Noting that the growth rate for KH instability is $\propto \sqrt{\rho_1 \rho_2}/(\rho_1 + \rho_2)$, the lower density and higher velocity in model Orbit-RD results in slower growth rates. Therefore, the flow exits the grid with fewer noticeable perturbations. But why does this difference occur? Consider the motion of postshock gas away from the stagnation point. In model Orbit-IA postshock gas is accelerated by the pressure gradient. However, in model Orbit-RD the postshock primary wind is of a low enough temperature to be acted upon by the radiation fields of the stars. Therefore, the higher velocity of postshock primary's wind in model Orbit-RD is due to radiative acceleration.

Examining the leading arm of the WCR the layer of postshock primary wind appears thicker in model Orbit-

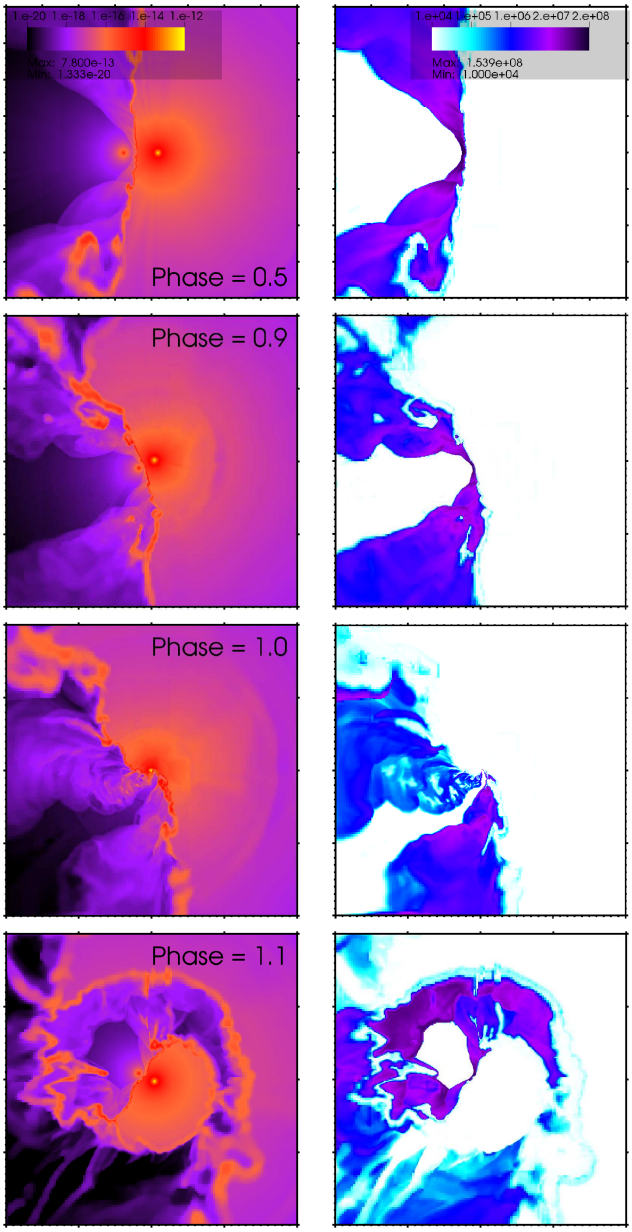

FIG. 8.— Snapshots of the gas density (left column) and temperature (right column) in the orbital ($x-y$) plane from model Orbit-IA at $\phi = 0.5$ (top row), 0.9 (upper middle row), 1.0 (lower middle row), and 1.1 (bottom row). The orbital motion of the stars is calculated in the centre of mass frame. At apastron ($\phi = 0.5$) the primary star is to the right, and the companion star is to the left, of the image centre. The motion of the stars proceeds in an anti-clockwise direction. All plots show a region of $\pm 2 \times 10^{15}$ cm - large axis tick marks correspond to a distance of 1×10^{15} cm.

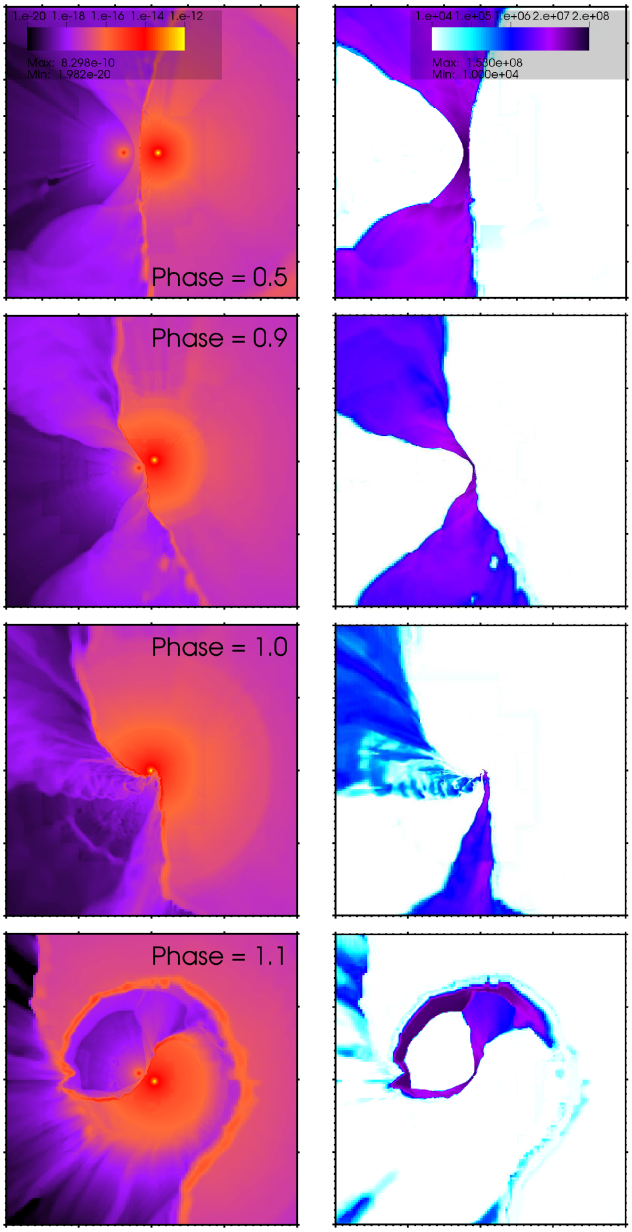

FIG. 9.— Same as Fig. 8 except model Orbit-RD is shown.

RD when compared to model Orbit-IA. Interestingly, at phases close to periastron when this gas resides close to the stars, its thermal pressure is lower than the radiation pressure, which provides resistance against contraction and thus widens the layer. However, comparing the snapshots at $\phi = 1.1$ we see that at an equivalent distance from the stars the density of the unshocked winds is slightly higher in model Orbit-RD, which means the mass in the swept-up shell is greater. The inertia of the swept-up mass is therefore greater in model Orbit-RD, which accounts for the smaller distance that the spiral has travelled to by $\phi = 1.1$ in this model compared to model Orbit-IA.

The width of the dense layer clearly affects the growth of instabilities in the expanding spiral-shaped shell - in model Orbit-IA the shell appears to be subject to the NTSI, whereas in model Orbit-RD the additional thickness to the layer renders it stable. This is unsurprising as the stability of an expanding shell depends on the shock thickness (Vishniac 1983; Wünsch et al. 2010). This raises questions about the fate of the expanding shell in each simulation. As its outwards acceleration is decreased by an increasing amount of swept up mass its Mach number will decrease and as the shocks dissipate it will gradually mix with the bubble of companion wind which it encases. However, this only appears to be

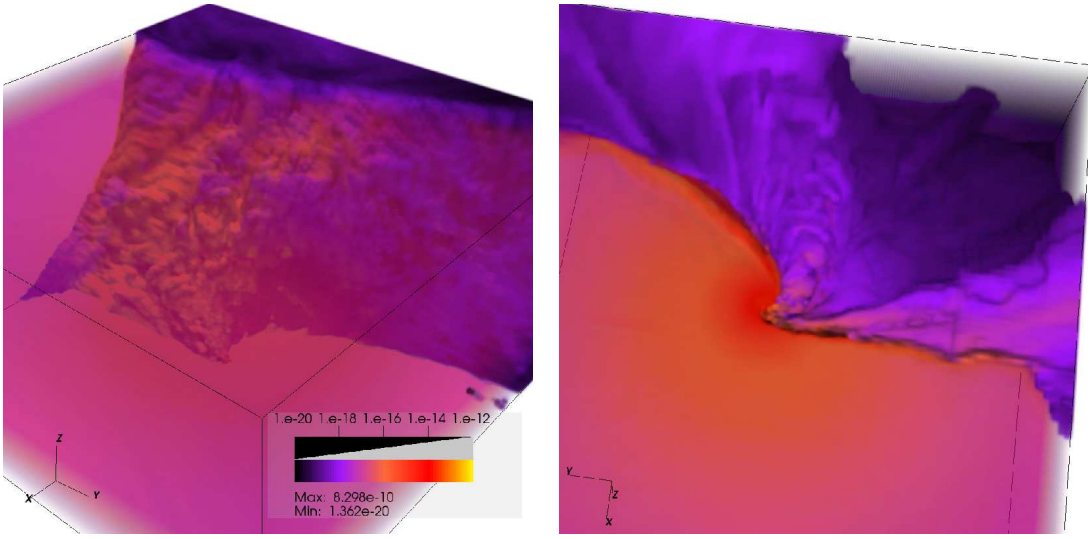

FIG. 10.— 3D gas density volume rendering of simulation Orbit-RD at periastron passage ($\phi = 1.0$) viewed from above (left panel) and below (right panel) the simulation box. The entire simulation domain is shown.

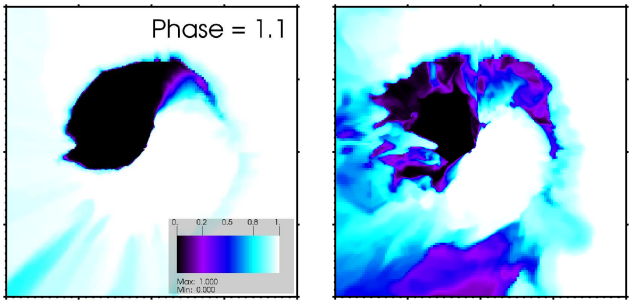

FIG. 11.— Snapshots of orbital ($x - y$) plane from simulation Orbit-RD (left panel) and Orbit-IA (right panel) at $\phi = 1.1$ showing the fluid dye variable. Values of 1 and 0 correspond to a cell consisting entirely of primary or companion wind material, respectively, and intermediate values indicate a mixture. The plots show a region of $\pm 2 \times 10^{15}$ cm - large axis tick marks correspond to a distance of 1×10^{15} cm. For the corresponding density and temperature images see Figs. 8 and 9.

the case for model Orbit-RD in certain directions. In the trailing arm of the WCR the dense layer of postshock primary wind is photo-ablated by the radiation fields. Yet, this only occurs in the trailing arm of the WCR because the dense layer can be driven into a more tenuous cavity made by the companion's wind as it swings through periastron. In contrast, the leading arm is bordered by unshocked primary wind, and therefore the dense layer is merely widened by the radiation pressure. Examining the fluid dye variable (which tracks the quantity of each wind in a given cell) the photo-ablation by the radiation fields of the stars appears to be a very effective mixing agent and (unlike in model Orbit-IA) smooth out any filamentary structure. Comparing models Orbit-RD and Orbit-IA at $\phi = 1.1$ we see that in the former the photo-ablation of the dense layer snips the tail of companion wind gas in the WCR (Fig. 11).

Following the expansion of the shell as it exits the system, we see that the shocked gas in the current spiral crashes through the remnant of the WCR from prior to periastron passage, and Richtmyer-Meshkov (RM) instabilities are formed at the interface between the two. The additional mixing provided by photo-ablation and the collision of successive expanding spiral-like shells will have implications for models of observations directly related to the postshock primary star's wind, e.g. forbidden line emission (Gull et al. 2009), episodic dust formation (Smith 2010), and high-velocity absorption features (Groh et al. 2010b).

5.1.2. *Periastron passage*

Focusing now on the periastron passage of η Car, where there is a considerable rate of change in the position of the stars and the distribution of the winds, a number of interesting features can be identified. Firstly, there appears to be a sudden change in the level of instability in the shocks as periastron is approached. For instance, prior to periastron the shocks seem to be unstable in both model Orbit-IA and Orbit-RD (see $\phi = 0.990$, and 0.995 snapshots in Figs. 12 and 13), and one sees that, consistent with the predictions of the periastron simulations in § 4, the postshock gas is more unstable when the wind acceleration regions are taken into consideration (model Orbit-RD) than in the case where they are not (model Orbit-IA). This fact is highlighted at $\phi = 0.995$ where in model Orbit-RD a shard of dense postshock primary wind gas is forced through the shocks by instabilities in the leading arm of the WCR and comes close to colliding against the companion star before being rapidly ablated by its wind. However, as $\phi = 1.000$ is approached, and the orbital velocities of the stars increase, the shocks directly between the stars appear much more stable and the catastrophic disruption of the WCR seen in model Peri-RD is not reproduced in model Orbit-RD. The reason for this is two-fold. Firstly, the level of radiative inhibition of the preshock companion's wind is not as severe when orbital motion is included - this point is discussed in more detail below. And secondly, orbital motion, and the velocity component that it provides perpendicular to the line of centres, increases the preshock velocity. Consequently, the postshock gas is less radiative and the prevailing thermal pressure stabilizes the WCR against the

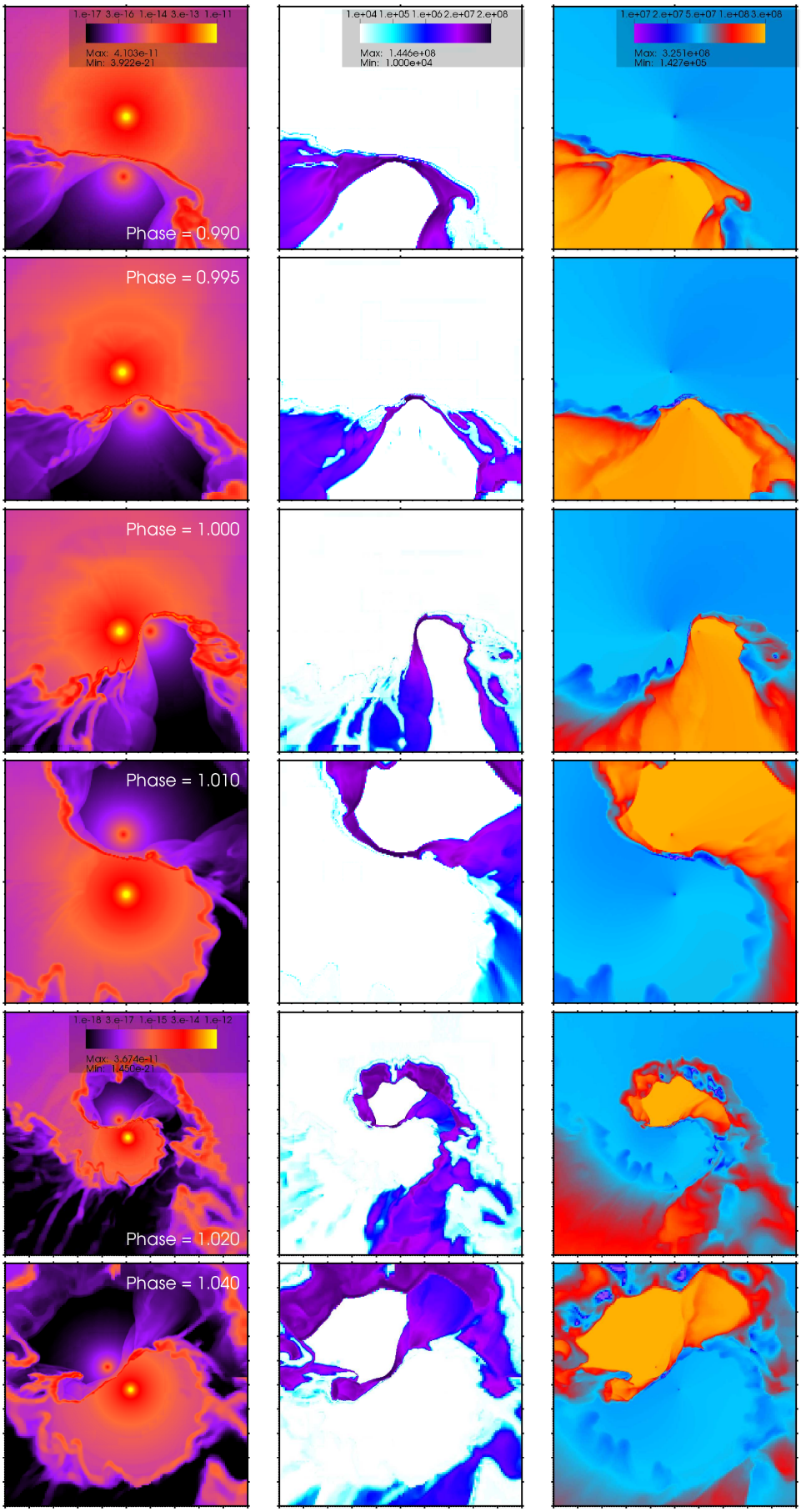

FIG. 12.— Snapshots of the orbital $(x - y)$ plane from model Orbit-IA showing (from top to bottom) $\phi = 0.990$, 0.995, 1.000, 1.010, 1.020, and 1.040, and (from left to right) density, temperature, and speed. At periastron ($\phi = 1.000$) the primary star is to the left, and the companion star is to the right, of the image centre. The plots at $\phi = 0.990$, 0.995, 1.000, and 1.010 show a region of $\pm 1 \times 10^{14}$ cm, whereas the plots at $\phi = 1.020$ and 1.040 show a region of $\pm 5 \times 10^{14}$ cm. In all plots large axis tick marks correspond to a distance of $\pm 1 \times 10^{14}$ cm. Note the difference in colour scale used for the density plots at ϕ =1.020 and 1.040.

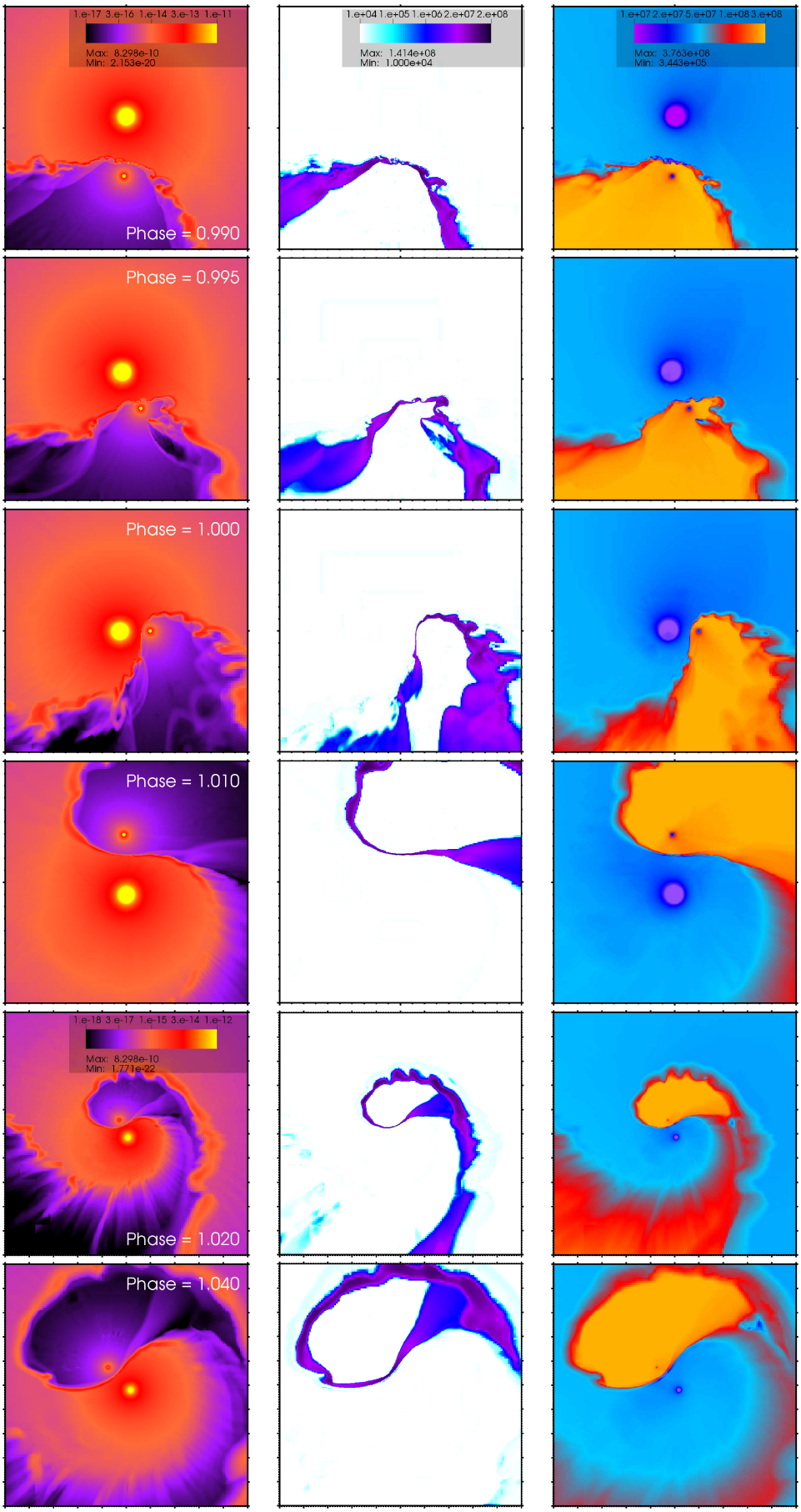

FIG. 13.— Same as Fig. 12 except model Orbit-RD is shown.

growth of NTSIs. These results imply that a significant disruption to the WCR must be afoot prior to the rapid rotation of the stars (i.e. prior to $\phi = 1.0$).

At orbital phases after periastron the contortion of the WCR by the motion of the stars is most evident. The snapshots at $\phi = 1.01$ and 1.02 in Figs. 12 and 13 show how the unshocked companion wind is completely enclosed by the WCR. Following periastron one can see that the arms of the WCR become twisted to such an extent that they collide downstream (see $\phi = 1.02$ in Figs. 12 and 13), so that postshock gas in the trailing arm is further heated as it passes through the shocks in the leading arm. The wind of the companion star (on the side facing away from the primary star) now collides against the inside of the leading arm of the WCR and helps to heat this gas. In model Orbit-RD the preshock companion wind in this direction is accelerated by the cumulative radiative driving force from both stars, the result of which is that immediately preshock this gas has reached a velocity of 3300 km s^{-1}, noteably higher than the (terminal) velocity of the companion wind in model Orbit-IA. Consequently, the ram pressure of the preshock gas is higher and it attains a pressure balance with the postshock gas at a larger distance from the companion star, causing the region of postshock companion wind to be thinner in model Orbit-RD compared to model Orbit-IA. However, despite the higher ram pressure of the companion's wind in this direction, the expansion of the spiral at this time occurs at roughly the same speed because the companion's wind is effectively running into a wall of dense postshock primary wind with a high inertia. Therefore, it is the postshock primary wind which largely dictates the rate of expansion. Examining the tail of the WCR in the density snapshots at $\phi = 1.01$, 1.02, and 1.04 one can see a striking example of photo-ablation by the radiation fields of the stars (see Fig. 13).

5.1.3. *Preshock velocities*

The simulations presented in § 4, in which the stars were static with a separation corresponding to periastron, predicted that the winds shock at such speeds that the WCR becomes very unstable, so that dense clumps of gas may collide with the companion star. Yet, when we add orbital motion to the mix we do not see a disruption of such magnitude. If anything, the rapid motion of the stars around periastron passage appears to have a stabilizing effect on the apex of the WCR. We can begin to dissentangle this puzzle by examining the preshock velocities from models Orbit-RD and Peri-RD (Fig. 7). Clearly, at orbital phases leading up to periastron the companion's wind is not reduced to the same preshock velocity in model Orbit-RD as in model Peri-RD. In fact, in model Orbit-RD the preshock companion's wind velocity does not decrease to that in model Peri-RD until $\phi \simeq 1.005$, at which point the lowest preshock velocity is attained. Following this phase the agreement between model Orbit-RD and Peri-RD improves and there appears to be a good correlation between the level of radiative inhibition occuring. This behaviour is due to the combination of two effects introduced by orbital motion (see Fig. 14). In the frame of the WCR, the preshock gas velocity is equal to the wind velocity (in the frame of the star) plus the relative velocity of the star along the line of centres, $\dot{d}_{\rm sep}$. Therefore, prior to $\phi \simeq 0.99$, $\dot{d}_{\rm sep}$ is positive and the contraction of the stellar separation will increase the preshock wind velocity. However, $\ddot{d}_{\rm sep}$ is positive until $\phi \simeq 0.99$ and then becomes negative (Fig. 14), so at $\phi > 0.99$ the radial motion will decrease the preshock wind speed. The wind material also has a considerable velocity in the transverse direction which increases (decreases) as the stars approach (depart from) periastron. This motion reduces the wind density along the line of centres, and as $g_{\rm rad} \propto \rho^{-\alpha}$ the wind acceleration increases, and the impact of radiative inhibition decreases (see Fig. 15). Note that the alteration to $g_{\rm rad}$ will apply for both radiation fields, but since $\alpha_2 > \alpha_1$ the reduction in ρ benefits the secondary's radiative driving more than inhibition by the primary.

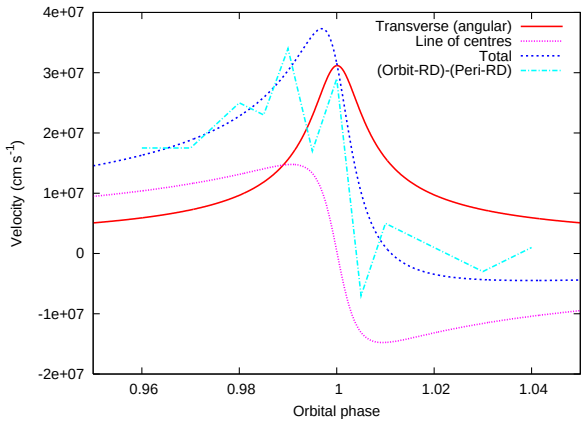

FIG. 14.— The orbital speed of the companion star around periastron passage. The components for the transverse and line-of-centres velocity, as well as the sum (total) are shown. For comparison, we also plot the difference between the preshock companion star wind velocities from models Orbit-RD and Peri-RD. Note that these values are calculated in the frame of reference of the centre of mass.

Prior to $\phi \simeq 1.01$ the combination of these two effects increases the companion's preshock wind speed along the line of centres compared to the static-star case (see Figs. 3 and 14). However, following periastron the enhanced preshock velocity introduced by transverse motion is countered by the receding relative motion of the companion star along the line of centres. Examining the sum of the orbital velocity components around periastron one sees good qualitative agreement with the difference between models Orbit-RD and Peri-RD (Fig. 14). We note that although the critical point radius of the wind acceleration is not resolved in the simulations, the influence of orbital acceleration on the preshock winds will be negligible (Appendix C).

In simulation Orbit-IA a maximum wind speed of ~ 3200 km s^{-1} is attained. When the acceleration of the winds by the radiation fields of both stars is considered the maximum speed for gas grows to ~ 4500 km s^{-1}, with the highest velocities possessed by unshocked companion wind gas which has been subjected to the cumulative driving force from both stars. Although velocities of this order will produce extremely hot gas when it shocks it is unlikely that there will be a significant observable signature as the total gas mass, its postshock density, and thus the free-free emission, is very low.

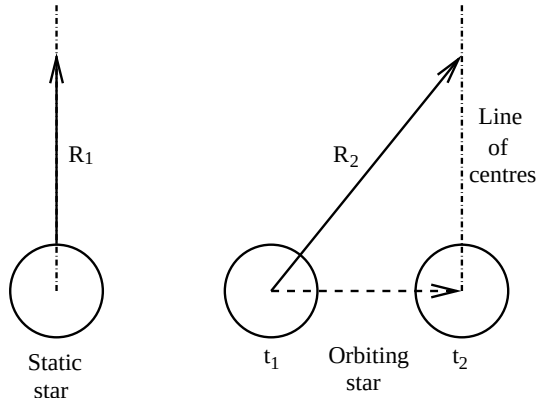

FIG. 15.— An illustrative example of the effect of orbital motion on the resultant line of centres wind acceleration. When the stars are static the line of centres (dot-dashed line) is aligned with radial flow (left). However, when a star undergoes orbital motion (right) the flow along the line of centres at time t_2 consists of wind material emitted at earlier times, t_1. Consequently, the path length for flow to reach the line of centres is larger (i.e. $R_2 > R_1$) and as $\rho \propto r^{-2}$ and $g_{\rm rad} \propto \rho^{-\alpha}$, this leads to an increase in the radiative acceleration.

5.1.4. *Resolution dependence*

Resolution tests were performed for the large-scale simulations using finest cell sizes (for the postshock gas) in the range $0.66 - 2.44 \times 10^{11}$ cm ($0.88 - 3.5$ R$_\odot$). As the simulation resolution is lowered the growth of KH instabilities at the contact discontinuity is less pronounced, and vice-versa for higher resolution. Importantly, there was a consistent finding that a substantial disruption/collapse of the WCR does not occur in simulations which include orbital motion (for our adopted stellar, system, and radiation-wind coupling parameters).

We note again that the key reason that a catastrophic disruption/collapse of the WCR does not occur at periastron in model Orbit-RD is that the companion's preshock wind velocity does not reach sufficiently low values to trigger radiative cooling in the postshock gas. Therefore, although the simulations are only progressed through a single orbit, continuing the simulation for subsequent orbits would not result in a disruption/collapse.

5.2. *X-ray emission*

η Car is an exceptionally bright source of X-ray emission. This X-ray emission provides a direct probe of the WCR, and detailed comparisons of model predictions against observations can determine key parameters of the stars and their winds. To date, considerable focus has been placed on constraining the orientation of the orbit on the plane of the sky. There remains a lack of consensus on this issue, with some models preferring the companion star to pass behind the primary star at periastron (Damineli 1996; Pittard et al. 1998; Corcoran et al. 2001; Pittard & Corcoran 2002; Corcoran 2005; Akashi et al. 2006; Hamaguchi et al. 2007; Nielsen et al. 2007; Henley et al. 2008; Okazaki et al. 2008; Parkin et al. 2009; Gull et al. 2009; Richardson et al. 2010; Groh et al. 2010b), whereas others prefer the orientation the opposite way around (Falceta-Gonçalves et al. 2005; Abraham et al. 2005a; Abraham & Falceta-Gonçalves 2007; Kashi & Soker 2008; Falceta-Gonçalves & Abraham 2009; Abraham & Falceta-Gonçalves 2010), or the system at quadrature (Ishibashi 2001; Smith et al. 2004). The inclination of the orbital plane, and whether or not it is aligned with the equatorial skirt of the Homunculus nebula, is still debated (see Parkin et al. 2009, and references there-in). Our new models can also be used to test the orientation. We define our line of sight geometry as follows: the inclination angle, i, is measured against the z-axis ($i = 0^\circ$ would view the system from directly above the orbital plane), and the angle θ is measured against the *negative* x-axis (companion star in front at apastron) such that θ increases in the prograde direction ($\theta = 90^\circ$ would align the line of sight with the negative y-axis). We adopt viewing angles of $i = 42^\circ$ and $\theta = 20^\circ$, in agreement with values determined from the most recent modelling of the X-ray emission from η Car (Okazaki et al. 2008; Parkin et al. 2009). In the following analysis we define $\phi = 1.0$, 2.0, and 3.0 as periastron passage in 1998, 2003.5, and 2009, respectively.

5.2.1. *X-ray lightcurves*

The X-ray lightcurves for models Orbit-IA and Orbit-RD are shown in Fig. 16. The characteristic shape of η Car's X-ray lightcurve (Corcoran et al. 2001; Corcoran 2005; Corcoran et al. 2010) is reproduced by the models; the X-ray flux remains relatively flat for the majority of the orbit ($\phi \simeq 0.05 - 0.7$) and then as the stars approach periastron there is a sharp increase in X-ray flux ($\phi \simeq 0.7 - 0.99$) followed by an abrupt decline to a minimum at periastron, and a recovery of the X-ray flux as the stars move away from periastron. The difference in apastron flux between models Orbit-RD and Orbit-IA is due to the WCR being closer to the primary star in the former (see § 5.1). Due to the slightly different wind densities at equivalent distances from the stars in models Orbit-IA and Orbit-RD we do not attempt to infer suggested alterations to model parameters which would improve the model fits. However, we note that on the whole the adopted wind momentum ratio provides good agreement between the model and the observed lightcurve.

Examining the orbital phase range $\phi = 0.9 - 1.1$ reveals some noteable differences between the observations and the models. Both model Orbit-IA and, to a lesser extent, model Orbit-RD overestimate the peak in *average* flux observed by *RXTE* prior to periastron. At $\phi = 1.0$ the models do not reach the same minimum in flux as the *RXTE* data. This is, at first, a somewhat puzzling result as previous models were able to reproduce the low flux level at $\phi = 1.0$ via an eclipse of the X-ray emission region (Okazaki et al. 2008; Parkin et al. 2009). However, inspection of the 2-5 keV broadband image at this phase reveals considerable emission from downstream gas in the tail of the WCR (Fig. 17). This emission predominantly comes from the trailing arm of the WCR with a weaker contribution from the downtream gas in the leading arm (see Fig. 18 - note that due to our adopted viewing angle the emission close to the apex in the *leading* arm is strongly absorbed by the intervening primary wind). This lack of agreement provides an important clue as to the nature of the X-ray minimum of η Car - to match the low flux level at $\phi = 1.0$ the apex of the WCR must be disrupted at a slightly earlier phase such that the disruption propagates out and removes the X-

ray emitting plasma in the trailing arm. The residual flux observed by *XMM-Newton*[5] at $\phi = 1.0$ could then be contributed by the X-ray emitting plasma in the leading arm of the WCR (i.e. in the downstream gas *behind* the companion star - Parkin et al. 2009). The flow time for the postshock companion star wind to be accelerated from the shock apex to point "A" in Fig. 18 is $\simeq 12$ days ($\delta\phi \simeq 0.006$), which suggests that the disruption of the WCR must be afoot by $\phi = 0.994$, in agreement with the 0-40 days proposed by Soker (2005) for the commencement of an accretion event (see also Akashi et al. 2006).

A key failing is that neither model reproduces the observed extended X-ray minimum. The X-ray flux from model Orbit-IA recovers by $\phi = 1.017$, whereas model Orbit-RD shows a slightly extended minimum with a recovery by $\phi = 1.025$. It would therefore seem that the width of the extended X-ray minimum cannot be reproduced when the spatial extent of the emitting region is taken into consideration, which poses difficulties for models based on an eclipse of the X-ray emission region (Okazaki et al. 2008, see also Parkin et al. 2009). A step is seen in the minimum of model Orbit-RD, which corresponds to lines of sight passing through the dense shell of postshock primary wind, although it is not as pronounced as in the model of Parkin et al. (2009). Encouragingly, the width of the X-ray minimum in model Orbit-RD agrees well with the less extended cycle 3 minimum observed by *RXTE* in 2009 (see lower right panel of Fig. 16). This result implies that in the previous two cycles the extended X-ray minimum resulted from a catastrophic disruption of the WCR, whereas the shorter duration of the recent minimum indicates that the WCR was not so severely disrupted the last time around.

5.2.2. *X-ray line profiles*

If the apex of the WCR is heavily disrupted the projected velocity along the lines-of-sight from high temperature, X-ray emitting postshock gas will be different. A high spectral resolution observation with *Chandra* found that at $\phi = 1.009$ there was a positive line shift (i.e. away from the observer) for the S XVI line, whereas S XV, Si XIV, and Si XIII had negative line shifts (Henley et al. 2008, see also Behar et al. 2007). In the absence of a stable WCR between the stars the higher excitation S XVI line could still have been emitted by hot postshock companion star wind *close to* the WCR disruption which (for our adopted viewing angle) is travelling away from the observer (labelled "B" in Fig. 18). The S XV, Si XIV, and Si XIII lines could then originate from lower temperature gas further downstream in the leading arm of the WCR (labelled "C" in Fig. 18), which is moving towards the observer, albeit at a steep angle, such that there will be a negative projected line shift.

5.2.3. *Column density*

The emission-weighted column densities[6] from models Orbit-IA and Orbit-RD appear to be largely similar for the majority of the orbit (Fig. 19), though model Orbit-IA shows a slower decline in column density in the orbital phase range 1.0-1.4. This difference is caused by the distribution of the dense layer of postshock primary wind in relation to the lines of sight to the X-ray emitting plasma (see Figs. 8, 9, 12, and 13). In model Orbit-IA the growth of KH instabilities at the contact discontinuity in the leading arm of the WCR distort the dense layer of postshock primary wind and push it into the path of X-rays as they exit the system, consequently increasing the column density. In contrast, the lack of KH instabilities in model Orbit-RD results in a more rapid decline in column density as the stars move away from periastron. Interestingly, the column density calculated from model Orbit-RD agrees very well with the results from the model used by Parkin et al. (2009), which did not allow dynamical instabilities.

The column densities derived from fits to *XMM-Newton* spectra in the 2-10 keV energy range (Hamaguchi et al. 2007) are also plotted in Fig. 19. At $\phi \simeq 1.47$ the models and the Hamaguchi et al. (2007) values are in good agreement, with a rather modest reduction of 1.15 required to align the models and observation. Our adopted viewing angle places the companion star in front of the primary at this orbital phase. Therefore, $N_{\rm H} \propto \dot{M}_2$, and the aforementioned reduction factor would bring the companion star mass-loss rate to a value of $1.2 \times 10^{-5}\,{\rm M}_{\odot}\,{\rm yr}^{-1}$. However, at phases close to periastron the column densities calculated from models Orbit-IA and Orbit-RD are noticeably higher than the Hamaguchi et al. (2007) values. During this part of the orbit there is a more complicated distribution of both the shocked and unshocked winds which lines of sight to the X-ray emitting plasma must pass through. Therefore, we cannot infer such a clear-cut reduction in mass-loss rates from a comparison between the models and the Hamaguchi et al. (2007) column densities. At face value, Fig. 19 implies that a reduction in the mass-loss rates of at least a factor of 2 is necessary, which gives lower limits to the mass-loss rates of $\dot{M}_1 = 2.4 \times 10^{-4}\,{\rm M}_{\odot}\,{\rm yr}^{-1}$ and $\dot{M}_2 = 7 \times 10^{-6}\,{\rm M}_{\odot}\,{\rm yr}^{-1}$. However, this seems unlikely, given other evidence for mass-loss rates greater than those assumed here (Hillier et al. 2001, 2006; van Boekel et al. 2003; Groh et al. 2010a), unless these estimates have in turn been "contaminated" by emission from the WCR. Another, perhaps more palatable way to reconcile the difference would be to invoke the presence of (X-ray) ionized gas close to the stars, which would reduce the opacity and thus allow for higher mass-loss rates. Alternatively, perhaps observationally derived column densities around periastron are suspect, due to the complexities of disentangling different spectral components, and/or the vagaries of fitting simpler plasma models to complicated systems (Antokhin et al. 2004; Pittard & Parkin 2010). For instance, any residual soft X-ray emission near η Car (unresolved to *XMM-Newton*) will reduce the apparent column density.

Despite the model column densities being higher than the observed values, we can extract some useful information from a comparison of the variation in column density as a function of orbital phase. For instance, the models and the Hamaguchi et al. (2007) values agree in that there is a sharp rise immediately prior to perias-

[5] During the deep minimum there will be some contamination from the cosmic background in the *RXTE* data.

[6] The emission-weighted column density (EWC) is calculated as $N_{\rm EWC} = \Sigma N_{\rm H} L_{\rm intX} / \Sigma L_{\rm intX}$, where $N_{\rm H}$ and $L_{\rm intX}$ are the column density and 1-10 keV intrinsic luminosity from a given line of sight, and the summation is over all sight lines (pixels) in the X-ray image.

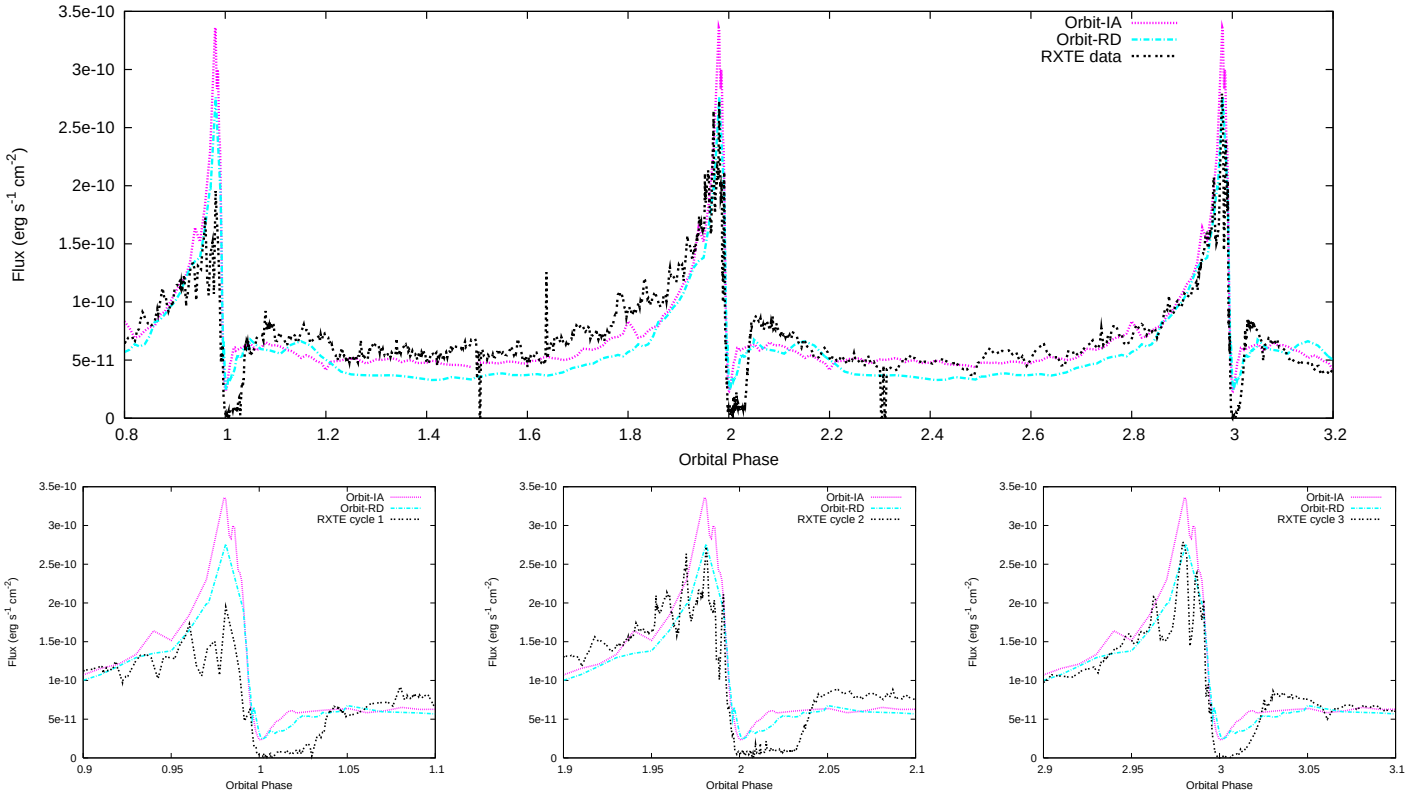

FIG. 16.— 2-10 keV X-ray lightcurves for models Orbit-IA and Orbit-RD plotted against the *RXTE* lightcurve over three cycles (top row) and against the individual minima (bottom row - left to right: 1998, 2003.5, and 2009). The estimated cosmic background has been removed from the *RXTE* data (Corcoran et al. 2001; Corcoran 2005; Corcoran et al. 2010).

FIG. 17.— Ray-traced images showing X-ray emission (erg s^{-1} cm^{-2} keV^{-1} ster) from model Orbit-RD at $\phi = 1.0$ in the 2-5 (left), 7-10 (middle), and 2-10 keV (right) energy bands. The centre of the image is aligned with the centre of the simulation box and the viewing angles are $i = 42°$ and $\theta = 20°$ (§ 5.2). The plots show a region of $\pm 4 \times 10^{14}$ cm - large axis tick marks correspond to a distance of 1×10^{14} cm.

tron which is followed by a dip, and then there is a second smaller peak. As shown by Parkin et al. (2009), the first peak ($\phi = 2.00$) corresponds to a rapid increase in absorption as the emission region is obscured by the dense unshocked primary's wind, and the second peak ($\phi = 2.02$) corresponds to sightlines to regions of high intrinsic luminosity becoming closely tangential with the leading arm of the WCR (see the $\phi = 1.02$ snapshots in Figs. 12 and 13). The differences between the time at which the EWC in the models and the data begin to increase as periastron is approached, and also the time of the peak in column, suggest that our adopted azimuthal angle $\theta = 20°$ is too small - if the value were increased slightly then the peak in column density would occur at a later orbital phase.

We note that in the model of Okazaki et al. (2008), which assumed the emission to originate from a point source situated close to the apex of the WCR, it was

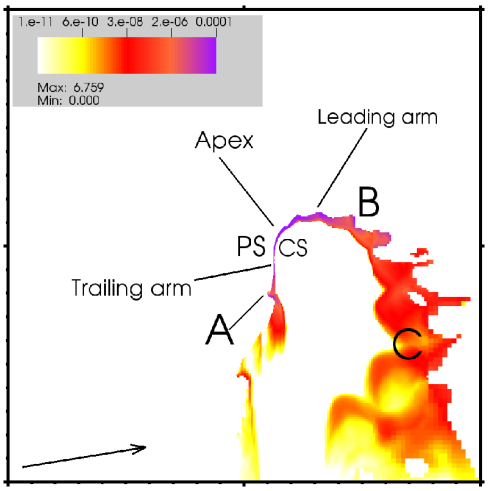

FIG. 18.— Snapshot of the orbital $(x-y)$ plane from model Orbit-RD at $\phi = 1.0$ showing the 2-5 keV X-ray emissivity (erg s^{-1} cm^{-3} keV^{-1} ster). The region of postshock gas in the trailing arm of the WCR responsible for the excess of 2-5 keV X-ray emission is labelled "A". The labels "B" and "C" refer to suggested sites for S and Si X-ray line emission. The position of the primary and companion star are indicated by the "PS" and "CS" labels, respectively. The arrow in the lower left of the image indicates the direction vector (in the orbital plane) for our adopted line of sight. The plots show a region of $\pm 1 \times 10^{14}$ cm - large axis tick marks correspond to a distance of 1×10^{14} cm. For the corresponding density, temperature, and speed images see Fig. 13.

this secondary peak in column density at $\phi = 2.02$ which allowed the extended X-ray minimum to be reproduced[7]. This is evident if one compares the position of the apex of the WCR relative to the leading arm of the WCR in the $\phi = 1.02$ and 1.04 snapshots in Figs. 12 and 13.

5.2.4. *Spectra*

X-ray spectra of η Car are particularly useful as they put tight constraints on the energy dependence of the X-ray emission from the postshock gas, which constrains the postshock gas temperature and the preshock velocity. Therefore, the spectra provide valuable clues as to the variation of the preshock companion's wind speed as a function of orbital phase.

In Fig. 20 we compare the X-ray spectra from models Orbit-IA and Orbit-RD to *XMM-Newton* spectra attained around periastron passage by Hamaguchi et al. (2007). To facilitate our comparison the non-variable emission components from the outer-ejecta, the X-ray Homunculus nebula, and the central constant emission component identified by Hamaguchi et al. have been removed, so that the remaining emission is almost entirely contributed by the WCR. At $\phi = 1.924$ the match between models Orbit-IA and Orbit-RD and the *XMM-Newton* spectrum appears quite good with only a slight overestimation (underestimation) of the flux at $E \lesssim 2$ keV ($E \simeq 3-7$ keV). The relative normalization of the models and the *XMM-Newton* spectra suggests that our adopted companion wind mass-loss rate is reasonable, whereas the slope of the 7-10 keV flux indicates that a slightly lower preshock companion wind speed is required at this phase.

The *XMM-Newton* spectra at $\phi = 1.988$ and 1.990 lie at the bottom and top of a flare-like feature, respectively. Therefore, the fact that both model Orbit-IA and Orbit-RD overestimate the flux level at $\phi = 1.988$ is unsurprising. Ideally, we would then like the models to slightly underpredict the observed flux level at $\phi = 1.990$ so that the *average* flux is approximately correct (i.e. neglecting the mechanism that produces the flare-like variability in the lightcurve). However, as the models are unable to reproduce the flare-like features in the observed lightcurve (Fig. 16), we take the level of agreement as reasonably good within the scope of the current investigation, and defer a detailed study of the flare-like features to future work.

Comparing the goodness of fit between the *XMM-Newton* spectra and the models presented in this work with the results of Parkin et al. (2009) we see a number of interesting details. Firstly, at orbital phases prior to periastron in cycle 2 ($\phi = 1.924, 1.988$, and 1.990) Parkin et al. showed that a reduced preshock companion star wind speed improved the agreement between the observed spectra and their model. However, we now find that even without any inhibition of the preshock companion's wind (model Orbit-IA) the fits to the spectra are considerably better. This implies that a more accurate description of the hydrodynamic structure of the WCR around periastron (i.e. the highly asymmetric temperature distribution in the leading and trailing arms - see Figs. 12 and 13) helps to account for the behaviour of the observed X-ray emission. In addition, our new model with modest radiative inhibition matches the spectra about as well as model Orbit-IA. This is because prior to $\phi = 0.990$ radiative inhibition of the preshock companion's wind is actually relatively minor.

The spectra taken at orbital phases during the extended X-ray minimum of cycle 2 ($\phi = 2.009$, 2.015, 2.018, and 2.023) are not well matched by the models, which overpredict the observed 7-10 keV flux by roughly an order of magnitude. Also apparent is the fact that the spectra do not drop off sharply as one tends towards lower energies. Examining the broadband images at these orbital phases shows that a significant amount of soft ($E \lesssim 3$ keV) X-ray emission originates from the tail of the WCR (see e.g. Fig. 17). In essence, there are two spatially discrete emission regions: the postshock gas near the apex of the WCR from which we only observe a significant flux of hard ($E \gtrsim 5$ keV) X-rays due to the obscuration by the primary's dense wind, and the downstream gas in the tail of the WCR which lies in the wake behind the companion star. The additional softer X-rays in model Orbit-IA at $\phi = 2.009$, 2.015, 2.018, and 2.023 compared to model Orbit-RD is therefore due to the higher level of instabilities in the tail of the WCR in the case of the former. Such instabilities perturb the dense layer of postshock primary wind into the path of the postshock companion's wind and in so doing they help to reheat the gas through a series of shocks - this is well illustrated by a comparison of the $\phi = 1.020$ snapshots in Figs. 12 and 13.

Parkin et al. (2009) found that an improved agreement between the model and data could be attained

[7] There was an additional source of absorption from a pile-up of unshocked primary wind gas in the SPH model of Okazaki et al. (2008). In our grid-based hydrodynamical models we do not see such a build-up as this gas is processed through the shocks and thereafter flows downstream within the WCR.

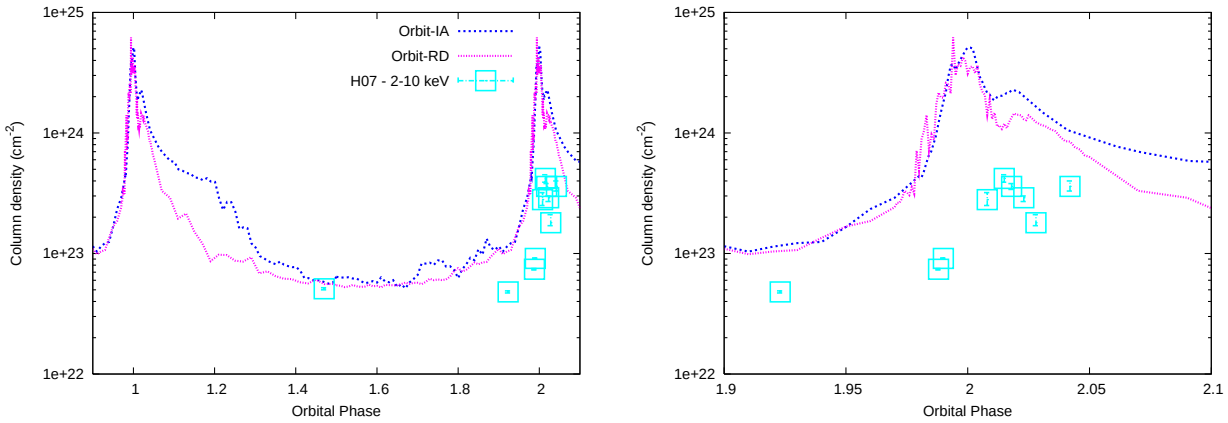

FIG. 19.— Emission weighted column density (EWC) for models Orbit-IA and Orbit-RD for orbital phase range $\phi = 0.9 - 2.1$ (left panel) and 1.9-2.1 (right panel). For comparison, the column densities derived by Hamaguchi et al. (2007) for the 2-10 keV X-ray emission are shown (H07 - 2-10keV), with the formal error bars obtained from spectral fitting. The interstellar and nebula column density ($\sim 5 \times 10^{22}$ cm^{-2}) are additional to these plots.

at $\phi = 2.009$ by either strongly inhibiting the preshock companion's wind to a velocity of 1600 km s^{-1} (not tested in this work), or via a disruption/collapse of the WCR. The net effect of these alterations was to reduce the 7-10 keV flux by a factor of roughly 10. Interestingly, a collapse/disruption of the shock apex may also help to resolve the problem with the excess emission at $E \lesssim 3$ keV by later modifying the conditions in the WCR further downstream. We note again that although a disruption/collapse of the WCR does not occur in model Orbit-RD, our adopted formalism for the coupling of the radiation fields to the opposing wind (Eq. 12) provides a lower limit to the degree of radiative inhibition of the companion's wind by the primary's radiation field. For instance, if we were instead to adopt k_2 and α_2 for the coupling of the companion's wind and the primary's radiation field the coupling would be stronger, and likewise the decelerative force would be greater. Therefore, the preshock companion's wind would be more strongly inhibited (see figure 21 of Parkin et al. 2009) and postshock gas would cool more rapidly making conditions more favourable for instability growth, and thus a disruption/collapse of the WCR.

Corcoran et al. (2010) compared *Chandra* X-ray spectra taken at roughly the same point during the 2003.5 and 2009 periastron passages, i.e. $\phi = 2.03$ and 3.03. Interestingly, the $\phi = 3.03$ spectrum showed an approximately identical shape to that at $\phi = 2.03$, albeit with a factor of ~ 12 higher flux level. Encouragingly, the models agree much better with the $\phi = 3.03$ spectra and support our conjecture that the lack of an extended WCR disruption/collapse is consistent with the recent periastron passage.

6. DISCUSSION

The simulations presented in § 4 of static stars at a separation corresponding to periastron (model Peri-RD) show that if the companion wind is suppressed sufficiently then the WCR displays catastrophic instabilities where dense clumps may hit the companion star. However, when orbital motion is included (§ 5, model Orbit-RD) the reduction in the preshock companion wind speed caused by radiative inhibition is smaller and higher preshock velocities stabilize the WCR. If one compares the results of simulations Peri-RD and Orbit-RD there appears to be a smoking gun for explaining the observed extended X-ray minima. The key lies in the radiative cooling of the postshock companion wind. We have argued that this can be brought about by the suppression of the preshock companion wind by radiative inhibition which, given our adopted relatively weak coupling between the primary's radiation field and the companion's wind, may not actually be such a hard thing to achieve. For example, the coupling between the radiation fields and the winds which we have adopted essentially provides a lower limit to the level of radiative inhibition which will be felt by the companion's wind (see § 3 and Fig. 3). In reality, the coupling between the radiation fields and the winds may lie somewhere between the two extremes of each star, and in that case a greater inhibiting force would be imparted on the preshock companion's wind by the primary's radiation field (Parkin et al. 2009). In addition, observations of massive star winds show them to be inhomogeneous (e.g. Fullerton et al. 1996; Markova et al. 2005; Davies et al. 2005; Moffat 2008), and the processing of clumps in the WCR could provide a sufficient density enhancement to trigger radiative cooling of the postshock companion's wind. Therefore, a useful direction for future investigations would be to perform simulations focused on periastron passage which explore a broader range of radiation-wind couplings and also the influence of inhomogeneous winds on the postshock gas conditions.

The factors which we mention in relation to triggering a disruption/collapse of the WCR may also help to explain the observed flare-like rapid variations in X-ray brightness. Moffat & Corcoran (2009) presented separate models based on clumps from the primary's wind entering the WCR and on an unstable WCR and found that each model had its fair share of difficulties reproducing the observations. Based on the results of models Peri-IA and Peri-RD, i.e. oscillations in the WCR causing rapid variations in the X-ray flux (Fig. 6), re-examining the combined rôle of instabilities and wind clumping using hydrodynamical models may be worthwhile. Furthermore, although relatively small clumps can be efficiently

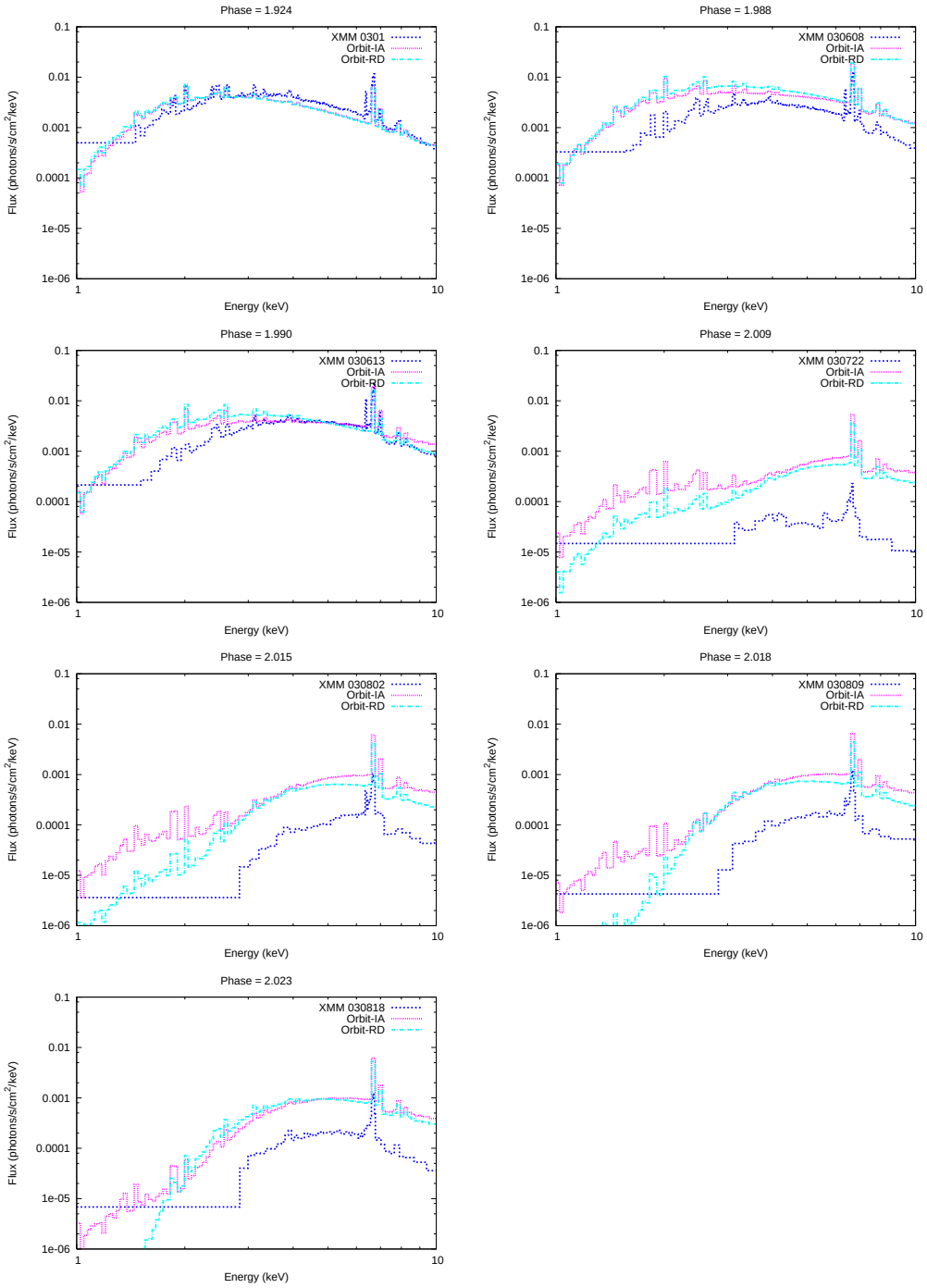

FIG. 20.— 1-10 keV X-ray spectra from models Orbit-IA and Orbit-RD at orbital phase (from top left to bottm right): $\phi = 1.924$, 1.988, 1.990, 2.009, 2.015, 2.018, and 2.023.

destroyed in largely adiabatic WCRs (Pittard 2007), this will not be the case for a radiative WCR. Large clumps traversing a highly unstable WCR consisting of radiative shocks may cause much greater variability, and could therefore account for the onset of large amplitude flare-like features as periastron is approached.

In model Peri-RD the clumps which collide with the companion star are removed from the computational domain when the wind is initiated after every time step. In reality, these clumps might disrupt the generation of the wind. While aspects of this scenario are reminiscent of the model proposed by Soker (2005), there are some crucial differences. In the Soker model the clumps originate in the preshock primary wind, whereas in model Peri-RD the clumps are formed by the fragmentation of the dense layer of postshock primary wind by the NTSI. Furthermore, in our work clumps do not traverse the shocks due to gravitational attraction, but instead are catapulted by violent instabilities. Since in our simulations the preshock stellar winds are mod-

elled as homogeneous, we cannot directly test Soker's model (although see Walder & Folini 2002; Pittard 2007; Parkin & Pittard 2010, for a discussion of the ablation of clumps in postshock flow).

Ideally, one would like to resolve the region around the stars such that the critical point radius of the wind acceleration region is well sampled. It is, however, a computationally demanding task to resolve the highly eccentric orbit of the stars and also the critical point radius (for the companion star this was $\sim 1.03\ R_{*2}$). It may therefore be advantageous in future models to adopt a sub-grid treatment of wind accretion which modifies the driving of the winds. For instance, "switching off" the initiation of the wind over those parts of the stellar surface in which the ram pressure of incident clumps exceeds that of the wind.

Photo-ablation by the stellar radiation fields clearly has important consequences for the fate of cool ($\sim 10^4$ K), dense postshock primary wind. With the stars in η Car being so immensely luminous, photo-ablation seems inevitable. However, in this work we adopted the CAK formalism for radiative driving, whereby the radiation-wind coupling is calibrated by the stars ability to drive its own wind. Therefore, the quantitative accuracy of future models would benefit from the use of a more suitable treatment of photo-ablation of circumstellar gas.

7. CONCLUSIONS

Three dimensional hydrodynamical simulations of the enigmatic super-massive binary star system η Car have been presented which include the radiative driving of the stellar winds, radiative cooling, gravity, and orbital motion. A suite of simulations were then performed to explore the rôle of wind acceleration, interacting radiation fields, and instabilities in the WCR on the gas dynamics and resulting X-ray emission. We summarize our key conclusions as follows:

- When one separates the coupling between the radiation fields of the stars and the opposing wind the level of radiative inhibition of the companion's wind is reduced. Consequently, in static-star calculations with a periastron separation the companion's wind attains a preshock velocity of $\simeq 2200$ km s^{-1} - notably higher than the estimate of $\simeq$ 1500 km s^{-1} when the radiation-wind couplings are not separated (Parkin et al. 2009).

- Despite a reduced level of radiative inhibition, when the wind acceleration regions are considered (in static-star calculations with a periastron separation) the WCR becomes massively disrupted by non-linear thin shell instabilities (NTSIs). This occurs because the lower preshock companion wind speed acquired due to wind acceleration and radiative inhibition leads to a lower postshock gas temperature. As such, radiative cooling becomes important in the postshock companion's wind and thermal pressure - which prevents the growth of the NTSI - is lost. The WCR is distorted to such an extent that dense fragments of cool postshock primary wind are repeatedly driven deep into the companion's wind acceleration region and in some instances collide against the star.

- When orbital motion is included the catastrophic disruption of the WCR is not reproduced. The root cause of this difference lies in the rapid orbital motion of the stars around periastron which acts to increase the preshock velocity, and thus postshock pressure, of the companion's wind. In so doing the stability of the WCR against thin-shell oscillations is increased. The influence of orbital motion will depend on the adopted system parameters.

- Large-scale, high resolution simulations show a number of interesting dynamical effects, including the influence of the stellar radiation fields on the growth of instabilities at the shocks, the photo-ablation of the cold dense layer of postshock primary wind, and the highly asymmetric temperature distribution in the arms of the WCR.

- The models provide a reasonable match to the majority of the *RXTE* lightcurve and, compared to previous models, the X-ray spectra agree much better with *XMM-Newton* observations obtained just prior to periastron. However, the extended X-ray minima are not reproduced by model Orbit-RD (which uses a relatively weak coupling between the primary's radiation field and the companion's wind) and the 7-10 keV X-ray emission is overestimated by roughly an order of magnitude. Yet, when the shock is heavily disrupted (in the static-stars simulation), the 7-10 keV X-ray luminosity of the postshock gas is an order of magnitude lower than the undisrupted case. This shows that dynamical instabilities in the WCR could be a key mechanism in explaining the X-ray observations.

- From a comparison between the model and *XMM-Newton* column densities around the 2003.5 periastron passage, a reduction of the stellar wind mass-loss rates by a factor of ~ 2 is implied. The revised mass-loss rates are $\simeq 2.4 \times 10^{-4}\,\mathrm{M}_\odot\,\mathrm{yr}^{-1}$ and $(7-12) \times 10^{-6}\ \mathrm{M}_\odot\,\mathrm{yr}^{-1}$ for the primary and companion wind, respectively. However, these estimates do not account for the possible presence of highly ionized, and thus lower opacity, gas close to the stars, and seem unlikely given other evidence for mass-loss rates greater than those assumed here (Hillier et al. 2001, 2006; van Boekel et al. 2003; Groh et al. 2010a). Alternatively, it may be that the observationally derived column densities around periastron are subject to uncertainty due to fitting simpler plasma models to complicated systems (see Pittard & Parkin 2010), and/or the process of disentangling different spectral components.

- To reproduce the extended minima likely requires effective radiative cooling in the postshock companion's wind close to the apex of the WCR. This could be achieved by stronger radiative inhibition of the preshock companion's wind (Parkin et al. 2009), albeit with a stronger radiation-wind coupling than explored in this work. If the companion's wind is sufficiently suppressed, or oscillations in the WCR are especially vigorous, a catastrophic

disruption/collapse of the WCR onto the companion star may occur.

We close with a note that the differences between the recent X-ray minimum and those previously observed could be accounted for by the stochastic nature of the growth of non-linear instabilities in the WCR. For example, we can speculate that the growth of instabilities in the 1998 and 2003 minima sufficiently disrupted the WCR to result in an extended quenching of the 7-10 keV X-ray emission. In contrast, during the shorter 2009 minimum the WCR was contorted by instabilities to a lesser degree, perhaps due to less significant radiative cooling of the postshock companion's wind, so that ultimately an extended disruption and/or collapse of the WCR against the companion star did not occur. This line of reasoning suggests that the differences between the most recent and the previous X-ray minima may be divided by a fine line related to the postshock gas conditions, and is an intriguing possibility given that multiwavelength observations suggest recent changes in the wind of η Car (Martin et al. 2010; Mehner et al. 2010b; Corcoran et al. 2010).

ACKNOWLEDGEMENTS

We thank Ian Stevens and Sven van Loo for helpful discussions, and the referee for useful suggestions which improved the presentation of this work. This work was supported in part by a Henry Ellison Scholarship from the University of Leeds, and by a PRODEX XMM/Integral contract (Belspo). JMP thanks the Royal Society for funding. This research has made use of NASA's Astrophysics Data System. This research has made use of data obtained from the High Energy Astrophysics Science Archive Research Centre (HEASARC) provided by NASA's Goddard Space Flight Center. Some of the software used in this work was in part developed by the DOE-supported ASC/Alliance Center for Astrophysical Thermonuclear Flashes at the University of Chicago. We thank the White Rose Grid and the UK National Grid Service (NGS) for use of their computer facilities.

REFERENCES

Abbott, D. C. 1980, ApJ, 242, 1183
Abdo, A. A. et al. 2010, arXiv:1008.3235
Abraham, Z., & Falceta-Gonçalves, D. 2007, MNRAS, 378, 309
—. 2010, MNRAS, 401, 687
Abraham, Z., Falceta-Gonçalves, D., Dominici, T., Caproni, A., & Jatenco-Pereira, V. 2005a, MNRAS, 364, 922
Abraham, Z., Falceta-Gonçalves, D., Dominici, T. P., Nyman, L., Durouchoux, P., McAuliffe, F., Caproni, A., & Jatenco-Pereira, V. 2005b, A&A, 437, 977
Agertz, O., et al. 2007, MNRAS, 380, 963
Akashi, M., Soker, N., & Behar, E. 2006, ApJ, 644, 451
Akashi, M., & Soker, N. 2010, arXiv:1006.3333v1
Anders, E., & Grevesse, N. 1989, Geochim. Cosmochim. Acta, 53, 197
Antokhin, I. I., Owocki, S. P., & Brown, J. C. 2004, ApJ, 611, 434
Behar, E., Nordon, R., & Soker, N. 2007, ApJ, 666, L97
Berger, M. J., & Oliger, J. 1989, Journal of Computational Physics, 53, 484
Castor, J. I. 1970, MNRAS, 149, 111
Castor, J. I., Abbott, D. C., & Klein, R. I. 1975, ApJ, 195, 157
Castor, J. L. 1974, MNRAS, 169, 279
Colella, P. & Woodward, P. R. 1984, Journal of Computational Physics, 54, 174
Corcoran, M. F. 2005, AJ, 129, 2018
Corcoran, M. F., & Hamaguchi, K. 2007, in Revista Mexicana de Astronomia y Astrofisica, vol. 27, Vol. 30, Revista Mexicana de Astronomia y Astrofisica Conference Series, 29–34
Corcoran, M. F., et al. 2004, ApJ, 613, 381
Corcoran, M. F., Ishibashi, K., Swank, J. H., & Petre, R. 2001, ApJ, 547, 1034
Corcoran et al. 2010, submitted
Cranmer, S. R., & Owocki, S. P. 1995, ApJ, 440, 308
Damineli, A. 1996, ApJ, 460, L49+
Damineli, A., et al. 2008a, MNRAS, 386, 2330
—. 2008b, MNRAS, 384, 1649
Damineli, A., Kaufer, A., Wolf, B., Stahl, O., Lopes, D. F., & de Araújo, F. X. 2000, ApJ, 528, L101
Davidson, K. 2002, ASPC, 262, 267
Davidson, K., & Humphreys, R. M. 1997, ARA&A, 35, 1
Davies, B., Oudmaijer, R. D., & Vink, J. S. 2005, A&A, 439, 1107
Dubey, A., Reid, L. B., Weide, K., Antypas, K., Ganapathy, M. K., Riley, K., Sheeler, D., & Siegal, A. 2009, arXiv:0903.4875
Duncan, R. A., & White, S. M. 2003, MNRAS, 338, 425
Falceta-Gonçalves, D., & Abraham, Z. 2009, MNRAS, 399, 1441
Falceta-Gonçalves, D., Jatenco-Pereira, V., & Abraham, Z. 2005, MNRAS, 357, 895
Ferland, G. J. 2000, in Revista Mexicana de Astronomia y Astrofisica Conference Series, Vol. 9, Revista Mexicana de Astronomia y Astrofisica Conference Series, ed. S. J. Arthur, N. S. Brickhouse, & J. Franco, 153–157
Ferland, G. J., Korista, K. T., Verner, D. A., Ferguson, J. W., Kingdon, J. B., & Verner, E. M. 1998, PASP, 110, 761
Fryxell, B., et al. 2000, ApJS, 131, 273
Fullerton, A. W., Gies, D. R., & Bolton, C. T. 1996, ApJS, 103, 475
Gayley, K. G., Owocki, S. P., & Cranmer, S. R. 1997, ApJ, 475, 786
Groh, J. H., Madura, T. I., Owocki, S. P., Hillier, D. J., & Weigelt, G. 2010a, ApJ, 716, L223
Groh, J. H., et al. 2010b, A&A, 517, 9
Gull, T. R., et al. 2009, MNRAS, 693
Hamaguchi, K., et al. 2007, ApJ, 663, 522
Henley, D. B., Corcoran, M. F., Pittard, J. M., Stevens, I. R., Hamaguchi, K., & Gull, T. R. 2008, ApJ, 680, 705
Hillier, D. J., Davidson, K., Ishibashi, K., & Gull, T. 2001, ApJ, 553, 837
Hillier, D. J., et al. 2006, ApJ, 642, 1098
Iping, R. C., Sonneborn, G., Gull, T. R., Massa, D. L., & Hillier, D. J. 2005, ApJ, 633, L37
Ishibashi, K. 2001, in Astronomical Society of the Pacific Conference Series, Vol. 242, Eta Carinae and Other Mysterious Stars: The Hidden Opportunities of Emission Spectroscopy, ed. T. R. Gull, S. Johannson, & K. Davidson, 53–+
Ishibashi, K., Corcoran, M. F., Davidson, K., Swank, J. H., Petre, R., Drake, S. A., Damineli, A., & White, S. 1999, ApJ, 524, 983
Ishibashi, K., et al. 2003, AJ, 125, 3222
Kaastra, J. S. 1992, Internal SRON-Leiden Report
Kashi, A., & Soker, N. 2008, MNRAS, 390, 1751
Kashi, A., & Soker, N. 2009a, MNRAS, 397, 1426
Kashi, A., & Soker, N. 2009b, ApJ, 701, L59
Leyder, J-C., Walter, R., & Rauw, G. 2008, A&A, 477, 29
—. 2010, arXiv:1008.5366
Lucy, L. B., & Solomon, P. M. 1970, ApJ, 159, 879
MacNeice, P., Olson, K. M., Mobarry, C., deFainchtein, R., & Packer, C. 2000, Comp. Phys. Comm., 126, 330
Markova, N., Puls, J., Scuderi, S., & Markov, H. 2005, A&A, 440, 1133
Martin J. C., Davidson K., Humphreys R. M., Mehner, A. 2010, AJ, 139, 2056
Mehner, A., Davidson, K., Ferland, G. J., & Humphreys, R. M. 2010a, ApJ, 710, 729
Mehner, A., Davidson, K., Humphreys, R. M., Martin, J. C., Ishibashi, K., Ferland, G. J., Walborn, N. R. 2010b, ApJ, 717, L22

Mewe, R., Kaastra, J. S., & Liedahl, D. A. 1995, Legacy, 6, 16
Moffat, A. F. J. 2008, in Clumping in Hot-Star Winds, ed. W.-R. Hamann, A. Feldmeier, & L. M. Oskinova, 17–+
Moffat, A. F. J., & Corcoran, M. F. 2009, ApJ, 707, 693
Nielsen, K. E., Corcoran, M. F., Gull, T. R., Hillier, D. J., Hamaguchi, K., Ivarsson, S., & Lindler, D. J. 2007, ApJ, 660, 669
Nielsen, K. E., Kober, G. V., Weis, K., Gull, T. R., Stahl, O., & Bomans, D. J. 2009, ApJS, 181, 473
Ohm, S., Hinton, J. A., & Domainko, W. 2010, ApJ, 718, 161
Okazaki, A. T., Owocki, S. P., Russell, C. M. P., & Corcoran, M. F. 2008, MNRAS, 388, L39
Owocki, S. P., & Gayley, K. G. 1995, ApJ, 454, L145+
Parkin, E. R., & Pittard, J. M. 2008, MNRAS, 388, 1047
—. 2010, MNRAS, 406, 2373
Parkin, E. R., Pittard, J. M., Corcoran, M. F., Hamaguchi, K., & Stevens, I. R. 2009, MNRAS, 394, 1758
Pauldrach, A., Puls, J., & Kudritzki, R. P. 1986, A&A, 164, 86
Pian, E., et al. 2009, arXiv:0908.2819
Pittard, J. M. 2007, ApJ, 660, L141
—. 2009, MNRAS, 396, 1743
Pittard, J. M., & Corcoran, M. F. 2002, A&A, 383, 636(PC02)
Pittard, J. M., & Parkin, E. R. 2010, MNRAS, 403, 1657
Pittard, J. M., Stevens, I. R., Corcoran, M. F., & Ishibashi, K. 1998, MNRAS, 299, L5+
Richardson, N. D., Gies, D. R., Henry, T. J., Fernández-Lajús, E., & Okazaki, A. T. 2010, AJ, 139, 1534
Smith, N., Gehrz, R. D., Hinz, P. M., Hoffmann, W. F., Hora, J. L., Mamajek, E. E., & Meyer, M. R. 2003, AJ, 125, 1458
Smith, N., Morse, J. A., Collins, N. R., & Gull, T. R. 2004, ApJ, 610, L105
Smith, N. 2010, MNRAS, 402, 145
Sobolev, V. V. 1960, Moving envelopes of stars (Cambridge: Harvard University Press, 1960)
Soker, N. 2005, ApJ, 635, 540
St-Louis, N., Moffat, A. F. J., Marchenko, S., & Pittard, J. M. 2005, ApJ, 628, 953
Stevens, I. R., Blondin, J. M., & Pollock, A. M. T. 1992, ApJ, 386, 265
Stevens, I. R., & Pollock, A. M. T. 1994, MNRAS, 269, 226
Strickland, R., & Blondin, J. M. 1995, ApJ, 449, 727
Tavani, M., et al. 2009, ApJ, 698, L142
Teodoro, M., Damineli, A., Sharp, R. G., Groh, J. H., & Barbosa, C. L. 2008, MNRAS, 387, 564
van Boekel, R., et al. 2003, A&A, 410, L37
van Genderen, A. M., Sterken, C., Allen, W. H., & Liller, W. 2003, A&A, 412, L25
Verner, E., Bruhweiler, F., & Gull, T. 2005, ApJ, 624, 973
Vishniac, E. T. 1983, ApJ, 274, 152
—. 1994, ApJ, 428, 186
Walder, R., & Folini, D. 2002, in Astronomical Society of the Pacific Conference Series, Vol. 260, Interacting Winds from Massive Stars, ed. A. F. J. Moffat & N. St-Louis, 595–+
Walter, R., Farnier, C., & Leyder, J. -C. 2010, arXiv:1008.2533
Whitelock, P. A., Feast, M. W., Koen, C., Roberts, G., & Carter, B. S. 1994, MNRAS, 270, 364
Whitelock, P. A., Feast, M. W., Marang, F., & Breedt, E. 2004, MNRAS, 352, 447
Wünsch, R., Dale, J. E., Palous, J., & Whitworth, A. P. 2010, MNRAS, 407, 1963

APPENDIX

A. INITIATING THE INSTANTANEOUSLY ACCELERATED WINDS

In simulations where the winds are instaneously accelerated we do not need to resolve the wind acceleration region. Therefore, the only resolution requirement comes from having a sufficent number of cells between the stars to accurately model the WCR dynamics. With this in mind, computational resources can be saved by making the radial distance into which the winds are initiated $R_{\rm map}$ a function of the separation of the stars,

$$R_{\rm map} = R_{\rm peri} \times 2^{l_{\rm peri}-l_\phi} \tag{A1}$$

where $R_{\rm peri}$ is a radial distance corresponding to approximately 10% of the distance between the stars at periastron (≥ 6 cells), l_ϕ is the number of nested levels of refinement required at a given orbital phase to accurately model the flow dynamics between the stars, and $l_{\rm peri} = l(\phi = 0.)$.

B. REFINEMENT CONDITION FOR POSTSHOCK GAS

To ensure that postshock gas is sufficiently well resolved to accurately describe the WCR dynamics we have implemented an additional criterion for grid refinement. Given the desired number of cells between the stars, $n_{\rm sep}$, the number of nested levels of refinement required at a given orbital phase

$$l_\phi = \log_2 \left(\frac{C_{\rm req}}{C_{\rm base}} \right), \tag{B1}$$

where $C_{\rm req} = d_{\rm sep}(\phi)/n_{\rm sep}$ is the resolution required, $d_{\rm sep}(\phi)$ is the separation of the stars, and $C_{\rm base}$ is the coarse grid resolution. For models Orbit-RD and Orbit-IA, $n_{\rm sep} \simeq 200$ cells.

C. ESTIMATING THE INFLUENCE OF ORBITAL ACCELERATION ON THE WIND

The motion of a star in an eccentric orbit introduces centripetal, $g_{\rm cen}$, and line-of-centres, $g_{\rm loc}$, accelerations. Considering the flow along the line of centres,

$$g_{\rm cen} = \frac{v_{\rm orb}^2}{R} = (1 + e\cos\omega) \left(\frac{M_{\rm orb}}{a(1-e^2)} \right)^{1/2}, \tag{C1}$$

and,

$$g_{\rm loc} = \frac{v_{\rm orb}}{R} \frac{2\pi a e \cos\omega}{P\sqrt{1-e^2}}, \tag{C2}$$

where $v_{\rm orb}$ is the orbital velocity, R is the radial distance to the system centre of mass ($= a(1-e^2)/(1+e\cos\omega)$), ω is the true anomaly ($= 2\pi\phi$), $M_{\rm orb}$ is the mass term relevant to the particular orbit under consideration (e.g. for

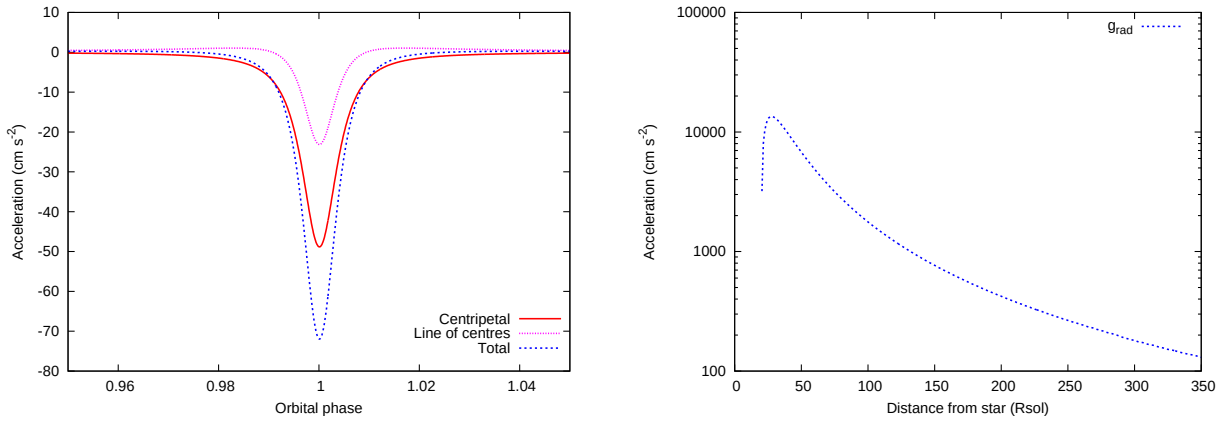

FIG. 21.— The orbital acceleration of the companion star around periastron passage (left panel) and the radiative line force calculated for the companion's single star wind profile (right panel). The components for the centripetal and line-of-centres, as well as the total are shown in the left panel. Note that these values are calculated in the frame of reference of the companion star (c.f. Fig 14).

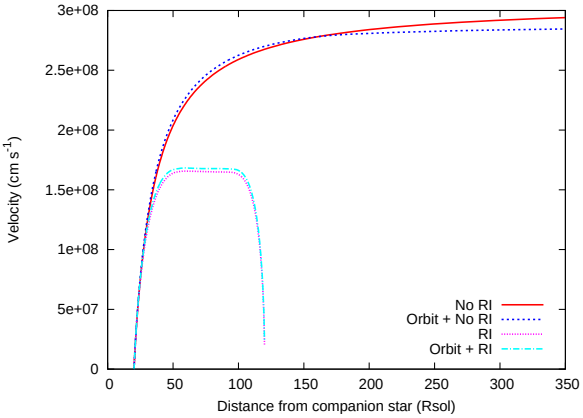

FIG. 22.— Companion star wind velocity along the line of centres between the stars. The primary star is situated at a distance of 359 $R_\odot$(corresponding to periastron separation when $e = 0.9$). The following solutions are shown: without radiative inhibition and orbital motion (No RI)(i.e. single star), without RI and with orbital motion (Orbit + No RI), with RI and without orbital motion (RI), and with RI and orbital motion (Orbit + RI). Dynamically consistent FDCFs have been used in these calculations (c.f. Eqs. C8 and C9). The orbital parameters are noted in Table 1, and stellar and line driving parameters are noted in Table 2.

the barycentric orbit of the companion star $M_{\rm orb} = GM_1^3/(M_1 + M_2)^2$), and P is the orbital period. The left panel of Fig. 21 shows $g_{\rm cen}$ and $g_{\rm loc}$ evaluated for the companion star of η Car. Comparing the acceleration due to orbital motion against the radiative line force calculated for the companion star one sees that the latter has a higher magnitude close to the star where the mass-loss rate is set (right panel of Fig. 21).

The influence of the orbital acceleration on the mass-loss rate and velocity profile of the wind can be estimated by incorporating $g_{\rm cen}$ and $g_{\rm loc}$ into the equation of motion

$$F(r, v, dv/dz) = \left(v - \frac{s^2}{v}\right)\frac{dv}{dr} + \frac{d\psi}{dr} - \frac{2s^2}{r} - g_{\rm rad} - g_{\rm orb}, \tag{C3}$$

where r is the distance from the centre of the star along the line-of-centres, s is the speed of sound, ψ is the gravitational potential, and $g_{\rm orb} = g_{\rm cen} + g_{\rm loc}$ is the orbital acceleration. The radiative line force, $g_{\rm rad}$ takes the form of Eq. 11. The value of $v_{\rm orb}$ at a given radius will depend on the time at which that parcel of gas left the star. However, as we are mainly interested in the affect of orbital motion on the base of the wind (i.e. where we initiate the winds in the hydrodynamic simulations), we neglect the radial dependence of $v_{\rm orb}$, and take $v_{\rm orb}(r) \approx v_{\rm orb}$. As the orbital acceleration is applied to the base of the wind we replace the R in the denominator of Eqs. C1 and C2 with $R - R_*$. Note that we do not use $R - r$ in the denominator as this would introduce an unrealistic singularity at the centre of mass of the binary system. To proceed, we make the coordinate transform using the substitution of variables (Abbott 1980),

$$u = \frac{-2GM_1(1-\Gamma_1)}{rs^2}; w = \frac{v^2}{s^2}; w' = r^2 v\frac{dv}{dr}[GM_1(1-\Gamma_1)]^{-1}, \tag{C4}$$

leading to

$$F(u,w,w') = \left(1-\frac{1}{w}\right)w' + h(u) - CB(u,w,w')w'^{\alpha}, \tag{C5}$$

where

$$B(u,w,w') = K_1(u,w,w') - \left(\frac{M_2\Gamma_2}{M_1\Gamma_1}\right)K_2(u,w,w')A(u), \tag{C6}$$

and

$$A(u) = \left(\frac{u_{\rm d}}{u-u_{\rm d}}\right)^2 \tag{C7}$$

with C given by equation (13) of Stevens & Pollock (1994). The FDCFs

$$K_1(u,w,w') = \frac{1-\left[1-\left(\frac{u}{u_*}\right)^2-\frac{2w}{w'u}\left(\frac{u}{u_*}\right)^2\right]^{1+\alpha}}{(1+\alpha)\left[1+\frac{2w}{w'u}\right]\left(\frac{u}{u_*}\right)^2}, \tag{C8}$$

and

$$K_2(u,w,w') = \frac{1-\left[1-\left(\frac{u}{u_*}\right)^2A(u)+\frac{2w}{w'u}\left(\frac{u}{u_*}\right)^2A(u)^{3/2}\right]^{1+\alpha}}{(1+\alpha)\left[1-\frac{2w}{w'u}A(u)^{1/2}\right]\left(\frac{u}{u_*}\right)^2A(u)} \tag{C9}$$

where $u_{\rm d} = u(d_{\rm sep})$, $u_* = u(R_*)$. The orbital motion terms, which only depend on r, are contained in the potential function,

$$h(u) = 1 + \frac{4}{u} - \frac{M_2(1-\Gamma_2)}{M_1(1-\Gamma_1)}A(u) + \frac{1}{u^2}\frac{u_{\rm orb}u_*}{u_*-u_{\rm orb}}\zeta, \tag{C10}$$

with

$$\zeta = \frac{2}{s^2}Rg_{\rm orb} = \frac{2}{s^2}\left(\frac{2\pi aev_{\rm orb}\cos\omega}{P\sqrt{1-e^2}} + v_{\rm orb}^2\right), \tag{C11}$$

where $u_{\rm orb} = u(R)$. The critical point of the wind profile is solved for using: i) the equation of motion $F(u,w,w') = 0$, ii) the singularity condition $\partial F/\partial w' = 0$, and iii) the regularity condition $\partial F/\partial u + w'\partial F/\partial w = 0$. The velocity gradient terms present in the FDCFs (Eqs. C8 and C9) require the solution for the wind profile to be attained using an iterative process, whereby monotonic FDCFs are used to attain an initial solution, then velocity gradient terms are included in subsequent iterations (Pauldrach et al. 1986).

Fig. 22 shows wind solutions for η Car with/without radiative inhibition and orbital motion, and calculated with a stellar separation corresponding to periastron. In these calculations $g_{\rm rad}$ has the form of Eq. 11, whereas in the hydrodynamic simulations $g_{\rm rad}$ has the form of Eq. 12. Hence, these calculations are intended to illustrate the qualitative effect of orbital acceleration on the wind. The inclusion of orbital motion slightly steepens the velocity profile close to the star. This is the opposite effect to stellar rotation, which causes a shallower velocity profile (Abbott 1980). Interestingly, neglecting radiative inhibition, the terminal wind velocity is lower when orbital motion is included. However, when radiative inhibition is included, and recalling that the WCR occurs at $\simeq 100\,{\rm R}_\odot$ from the companion star (at periastron and along the line of centres) in model Orbit-RD, there is a minor increase in the preshock velocity. Examining the critical point radius and mass-loss rate we find reduction factors of 0.12 % and 2.3 %, respectively. Therefore, orbital acceleration contributes a negligible difference in comparison to the interplay between the radiation fields and the gravity of the stars.